

The Future in Neutrino Oscillation Physics

Superbeams and Neutrino Factories

Jordi Burguet Castell

Research Work Report

2003

University of Valencia

CONTENTS

1. <i>Introduction</i>	1
1.1 Overview	1
1.2 Historical Context	1
1.2.1 Discovery of the Neutrino	1
1.2.2 The Solar Neutrino Problem	2
1.2.3 The Atmospheric Neutrino Problem	7
1.3 Theoretical Framework	10
1.3.1 Neutrino Flavors	10
1.3.2 Dirac and Majorana	11
1.3.3 Neutrino Mass	12
1.3.4 Mixing	13
1.3.5 Matter Effects	16
2. <i>Measuring the Mixing Parameters and Masses</i>	19
2.1 Main experimental lines	19
2.2 Reactor Experiments	22
2.3 Accelerator Experiments	23
2.3.1 K2K	23
2.3.2 NuMI	25
2.3.3 CNGS	25
2.4 Status as 2003	26
3. <i>The Ultimate Machine: Neutrino Factory</i>	29
3.1 Origin of the Idea	29
3.2 Characteristics	29
3.3 General Design	30
3.4 Muon Beams, Fluxes and Rates	32
3.5 Wrong Sign Muons	34
3.6 Detection	35
3.6.1 A Large Magnetized Calorimeter	35
3.7 Oscillation Physics at the Neutrino Factory	36

3.7.1	Oscillation Probabilities in Matter	37
3.7.2	Precision Measurement of Known Oscillations	38
3.7.3	Sensitivity to θ_{13}	38
3.7.4	Sensitivity to CP violation	39
3.8	Propaganda	40
4.	<i>Near Future: Superbeams</i>	41
4.1	Rationale	41
4.2	Generation of Superbeams	42
4.3	The SPL neutrino beam	43
4.4	Detection	43
4.4.1	Water Cerenkov Detectors	45
4.5	Sensitivity	45
4.5.1	Sensitivity to the Atmospheric Parameters	46
4.5.2	Sensitivity to CP violation	46
5.	<i>Correlations, Degeneracies, Combinations</i>	49
5.1	Correlations	49
5.2	Degeneracies	49
5.3	Status at the Neutrino Factory	50
5.3.1	Correlation Between δ and θ_{13}	52
5.3.2	Intrinsic Degeneracies	53
5.3.3	Simultaneous Determination of δ and θ_{13}	56
5.4	Combinations	58
5.4.1	Neutrino Factory with Superbeam	59
5.4.2	Resolution of Intrinsic Degeneracies	59
5.4.3	$\text{sign}(\Delta m_{23}^2)$ Degeneracy	65
5.4.4	$\theta_{23} \rightarrow \pi/2 - \theta_{23}$ Degeneracy	70
5.4.5	The Silver Channels	76
6.	<i>Conclusion</i>	78
7.	<i>Acknowledgements</i>	80
	<i>Appendix</i>	84
A.	<i>Program Architecture and Computer-Related Tools</i>	86
A.1	Numerical Simulations	86
A.2	Implementation	86
A.3	Architecture	87

A.3.1	Generation of Data	87
A.3.2	Reconstruction	87
A.4	Software Tools	88
A.5	Availability	88

1. INTRODUCTION

1.1 Overview

Neutrino physics have recently provided the first evidence of physics beyond the Standard Model. The most appealing explanation of a whole set of neutrino experiments carried out during the last 30 years, including the revolutionary Super-Kamiokande atmospheric neutrino data, is the existence of neutrino oscillations.

Neutrino oscillations imply that neutrinos do have mass. It also introduces a mixing matrix, similar to the CKM-matrix in the quark sector, which carries with it 4 new fundamental parameters: 3 mixing angles and the exciting possibility of a complex phase that would be responsible for leptonic CP violation.

The objective of the new generation of neutrino experiments is precisely a complete understanding of the parameters that govern their mixing, including neutrino masses and leptonic CP violation.

1.2 Historical Context

1.2.1 Discovery of the Neutrino

The neutrino appears for the first time in 1930, as an hypothesis formulated by Wolfgang Pauli [1] to explain the continuum energy spectra of electrons in the β decay. In radioactive decays, nuclei of atoms mutate into different nuclei when neutrons are transformed into protons, which are slightly lighter, with the emission of electrons, $n \rightarrow p e^- \bar{\nu}$.

Without the neutrino, energy conservation requires that the electron and proton share the energy of the neutron in a fixed amount, giving a monochromatic electron peak. This is not what was observed. Experiments indicated conclusively that the electrons were not mono-energetic, but could take a range of energies (see Fig. 1.1). This energy range corresponded exactly to the many ways the three particles in the final state of a three-body decay can share energy satisfying conservation of energy and momentum, if the third particle was very light. Pauli required his hypothetical particle to be neutral and have spin 1/2, to ensure conservation of electric charge and angular momentum respectively.

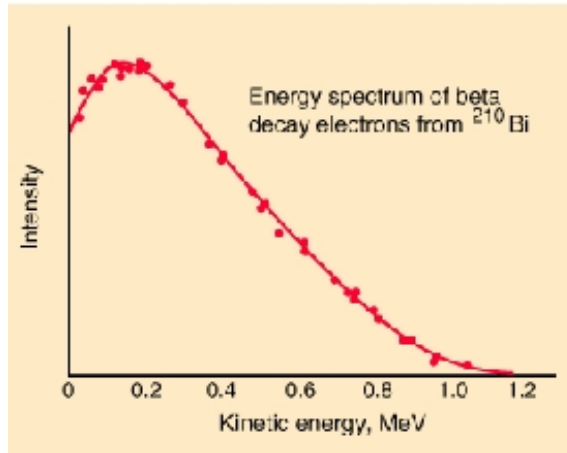


Fig. 1.1: The wide energy spectrum of the outgoing electron in the beta decay $n \rightarrow p e^- \bar{\nu}_e$ is in contradiction with the mono-energetic electron expected from a two body decay, and thus points to the existence of a third particle produced, which we know today to be the *electron antineutrino*, $\bar{\nu}_e$

Learning of Pauli's idea, Fermi proposed in 1934 his theory of beta decay, based on which Bethe & Peierls predicted in the same year the cross section for the interaction of the neutrino with matter to be extremely small.

In 1956, Cowan and Reines discovered the electron antineutrino through the reaction $\bar{\nu}_e p \rightarrow e^+ n$ using an experimental setup that they had proposed themselves three years before [2]. For this discovery they got the Nobel Prize 39 years later.

That same year, Pontecorvo, influenced by the recent study of Gell-Mann and Pais about the existence of neutral kaons, considered the possibility of a quantum mixture in the neutrino. In his work [3], he proposed that an antineutrino produced in the reactor of Savannah (Georgia, USA) could oscillate into a neutrino and this one be detected. That is how the theory of neutrino oscillation was born.

In 1962 Danby et al. observed the existence of different types of neutrinos, and the same year Maki, Nakagawa and Sakata introduced a key concept in the theory of oscillations: two different types of neutrinos can only oscillate between them if they have different masses [4].

1.2.2 The Solar Neutrino Problem

Solar neutrinos are electron neutrinos produced in the thermonuclear reactions that take place in the Sun. These reactions occur via two main chains, the proton-proton

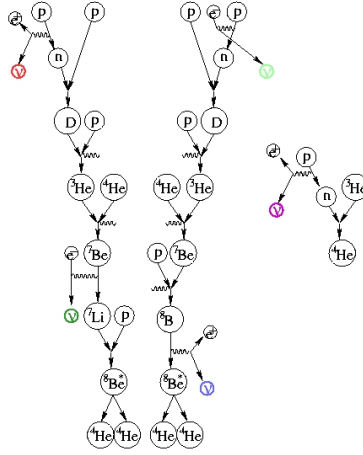
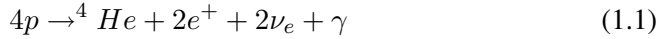


Fig. 1.2: The proton-proton chain, Sun's main source of energy, produces electron neutrinos.

chain (or PP chain) and the CNO cycle, shown in Figs. 1.2 and 1.3 respectively. The proton-proton chain is more important in stars the size of the Sun or less. There are five reactions which produce ν_e in the proton-proton chain, and three in the CNO cycle. Both chains result in the overall fusion of protons into ${}^4\text{He}$:



where the energy released in the reaction, $Q = 4m_p - m_{{}^4\text{He}} - 2m_e \simeq 26 \text{ MeV}$, is mostly radiated through the photons, and only a small fraction is carried by the neutrinos, $\langle E_{2\nu_e} \rangle = 0.59 \text{ MeV}$.

Solar Models [5] describe the properties of the Sun and its evolution after entering the main sequence. The models are based on a set of observational parameters: the surface luminosity, the age, radius and mass, and on several basic assumptions: spherical symmetry, hydrostatic and thermal equilibrium, equation of state of an ideal gas, and present surface abundances of elements similar to the primordial composition. With such models it is possible to predict the neutrino fluxes from the Sun, as well as their energy spectrum.

Raymond Davis, Jr., John Bahcall, and Don Harmer (Fig. 1.4) proposed in 1964 an experiment to search for solar neutrinos ${}^8\text{B}$ using a tank full of chlorine. Soon after, Davis started his historical experiment at the Homestake mine (South Dakota, USA) [6]. He received the 2002 Nobel Prize for pioneering contributions in the detection of cosmic neutrinos.

Four years later, Davis and his collaborators informed of a deficit in the flux of

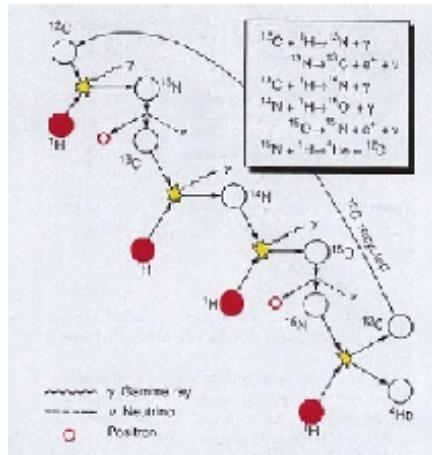


Fig. 1.3: CNO cycle in the Sun.

solar neutrinos when the obtained data were compared with the predictions of the Standard Solar Model (SSM) defined by Bahcall *et al.* [5]. (Davis received last year's Nobel Prize for pioneering contributions in the detection of cosmic neutrinos.)

The disagreement was called the “solar neutrino anomaly”, the “solar neutrino problem” and even the “mystery of the missing neutrinos”; it was thought that something was wrong either with the experiment or the SSM. However, Grivob and Pontecorvo interpreted this deficit as a clear evidence of neutrino oscillation.

Over the next twenty years many different possibilities were examined, but both the SSM and the experiment appeared to be correct. The solar models have been steadily refined as the result of increased observational and experimental information about the input parameters (such as nuclear reaction rates and the surface abundances of different elements), more accurate calculations of constituent quantities (such as radiative opacity and equation of state), the inclusion of new physical effects (such as element diffusion), and the development of faster computers and more precise stellar evolution codes.

The Davis experiment has been operating since, and five other experiments have joined in, GALLEX (Gran Sasso, Italy) [8], SAGE (Baksan, Rusia) [9], Kamiokande and Super-Kamiokande (Kamioka, Japan) [10], and most recently Sudbury Neutrino Observatory (SNO) (Sudbury, Canada) [11]. Each experiment is different from each other in that it observes an specific part of the solar neutrino spectrum (Fig. 1.5). All of them have found fewer ν_e than predicted by the Standard Solar Model (Fig. 1.6).



Fig. 1.4: Shortly after the proposal in 1964 that a ^{37}Cl solar neutrino experiment was feasible, three of the people most involved were photographed in front of a small version of the chlorine tank. From right to left, they are: Raymond Davis, Jr., John Bahcall, and Don Harmer.

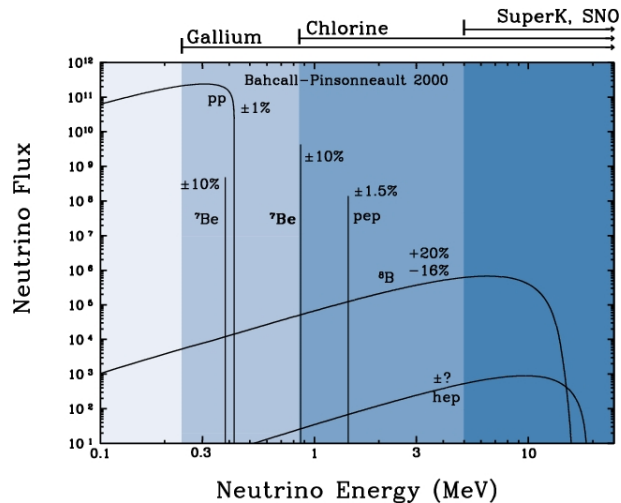


Fig. 1.5: Sensitivities of the different kind of solar neutrino experiments to the energy of the electron neutrinos produced in different reactions in the Sun.

Total Rates: Standard Model vs. Experiment
Bahcall–Pinsonneault 2000

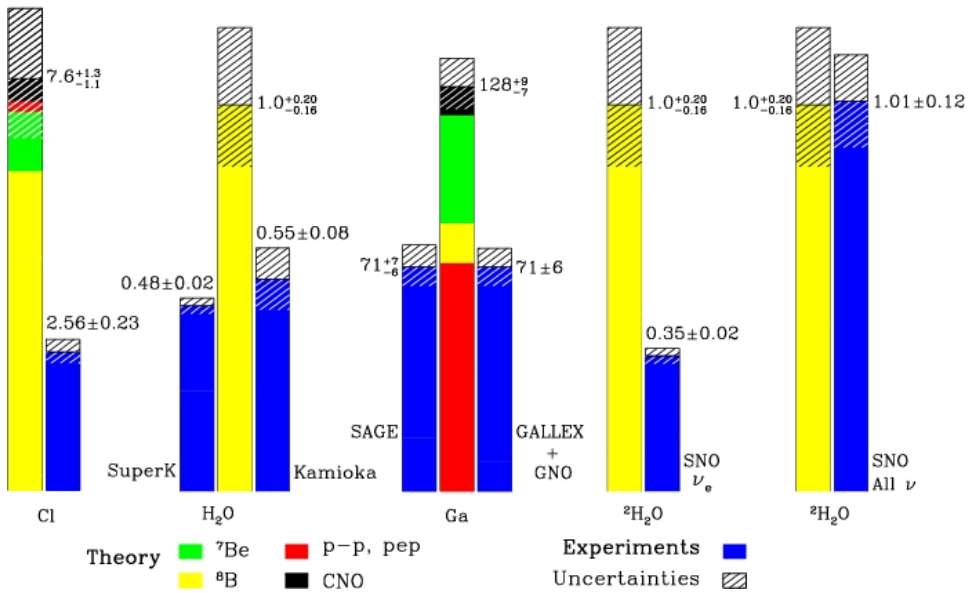


Fig. 1.6: Predictions of the Standard Solar Model with the total observed rates in the six solar neutrino experiments: Davis' chlorine, Super-Kamiokande, Kamiokande, GALLEX, SAGE, and SNO. The model predictions are color coded with different colors for the different predicted neutrino components. For both the experimental values and the predictions, the 1σ uncertainties are indicated by cross hatching.

Before the neutral current measurements at SNO all experiments observed a flux that was smaller than the SSM predictions, $\Phi^{obs}/\Phi^{SSM} \sim 0.3 - 0.6$. Also, the deficit is not the same for the various experiments, which may indicate that the effect is energy dependent. Those are the results that constitute what is called the “Solar Neutrino Problem”.

1.2.3 The Atmospheric Neutrino Problem

Atmospheric neutrinos are the neutrinos produced in cascades initiated by collisions of cosmic rays with the Earth’s atmosphere (see Fig. 1.7). Some of the mesons produced in these cascades, mostly pions and some kaons, decay into electron and muon neutrinos and antineutrinos:

$$\begin{aligned}\pi^\pm &\rightarrow \mu^\pm \nu_\mu (\bar{\nu}_\mu) \\ \mu^\pm &\rightarrow e^\pm \nu_e \bar{\nu}_\mu (\bar{\nu}_e \nu_\mu)\end{aligned}\quad (1.2)$$

The expected flux of atmospheric neutrinos depends on three main factors: the spectrum and composition of the cosmic rays, Earth’s geomagnetic field and the neutrino production cross-sections in the hadronic interactions that take place in the atmosphere. The fluxes are uncertain at the 20% level, but the ratios of neutrinos of different flavor are expected to be accurate to better than 5%. That’s why the experiments with atmospheric neutrinos typically present their results as a double quotient of the experimental values and the Monte Carlo predictions:

$$R = \left(\frac{N_\mu}{N_e} \right)_{exp} / \left(\frac{N_\mu}{N_e} \right)_{MC} \quad (1.3)$$

Atmospheric neutrinos were first detected in the 1960’s by the underground experiments in South Africa and the Kolar Gold Field experiment in India. These experiments measured the flux of horizontal muons (they could not discriminate between downgoing and upgoing directions) and although the observed total rate was not in full agreement with theoretical predictions, the effect was not statistically significant.

In the 1970s, with the appearance of the Grand Unification Theories (GUTs) and of the symmetries between leptons and quarks, it was suggested that the proton might be unstable. This originated the development of several underground detectors (to minimize the contamination originated by the products of the cosmic rays) big enough to manipulate many protons and detect the Cerenkov radiation emitted by the products of their decay. Two different detection techniques were employed. In water Cerenkov detectors the target is a large volume of water surrounded by

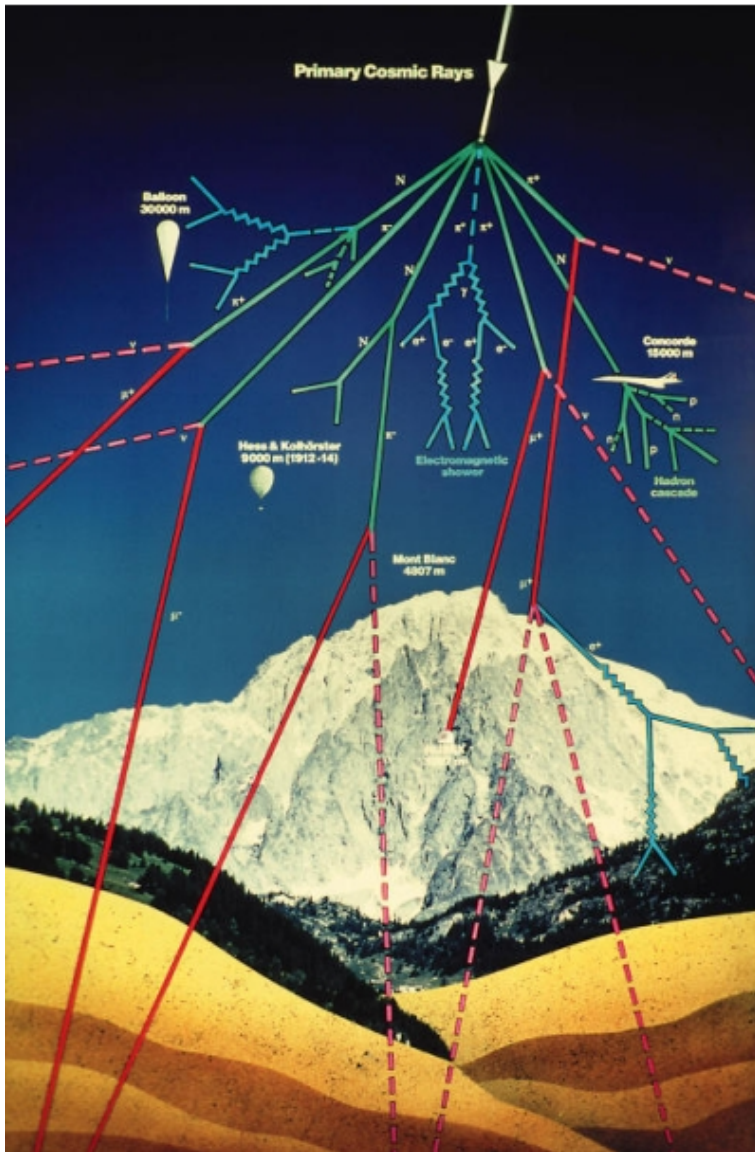


Fig. 1.7: A high-energy particle coming from space, a cosmic ray, interacts with an atom in the Earth's atmosphere and develops a cascade of particles. Some of the final particles are neutrinos.

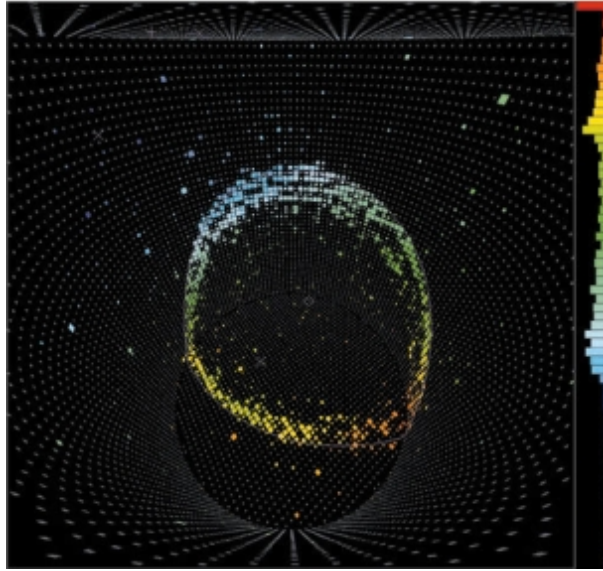


Fig. 1.8: Cerenkov ring produced by a neutrino interaction in water.

photomultipliers which detect the Cerenkov ring produced by the charged leptons (see Fig. 1.8). The event is classified as an electron-like or muon-like if the ring is respectively diffuse or sharp. In iron calorimeters, the detector is composed of a set of alternating layers of iron which act as target and some tracking element (such as plastic drift tubes) which allows the reconstruction of the shower produced by the electrons or the tracks produced by muons. Both types of detectors allow for flavor classification of the events.

The two oldest iron calorimeter experiments, Fréjus and NUSEX, found atmospheric neutrino fluxes in agreement with the theoretical predictions. On the other hand, two water Cerenkov detectors, IMB and Kamiokande, detected a ratio of ν_μ -induced events to ν_e -induced events smaller than the expected one by a factor of about 0.6. This was the original formulation of the atmospheric neutrino anomaly, or the “atmospheric neutrino problem”.

Whether $R_{\mu/e}/R_{\mu/e}^M$ is small because there is ν_μ disappearance of a ν_e appearance or a combination of both could not be determined. Furthermore, the fact that the anomaly appeared only in water Cerenkov and not in iron calorimeters left the window open for the suspicion of a possible systematic problem as the origin of the effect.

Kamiokande also presented the zenith angular dependence of the deficit for the multi-GeV neutrinos. The results seemed to indicate that the deficit was mainly

due to the neutrinos coming from below the horizon. Atmospheric neutrinos are produced isotropically at a distance of about 15 km above the surface of the Earth. Therefore neutrinos coming from the top of the detector have travelled approximately those 15 km before interacting while those coming from the bottom of the detector have traversed the full diameter of the Earth, $\simeq 10^4$ km before reaching the detector. The Kamiokande distribution suggested that the deficit increases with the distance between the neutrino production and interaction points.

The results of Kamiokande were later strongly confirmed by its successor, Super-Kamiokande. The data from Super-Kamiokande show that the angular and energy dependence of the ν_e spectrum corresponds to the expected one (with no oscillations). On the other hand, the ν_μ spectrum showed a strong dependency in the azimuthal angle. This is a clear evidence of ν_μ disappearance due to their oscillation to other neutrino flavor not detected.

1.3 Theoretical Framework

1.3.1 Neutrino Flavors

In the Standard Model, the strong, weak and electromagnetic interactions are related to, respectively, the $SU(3)$, $SU(2)$ and $U(1)$ gauge groups. Many features of the various interactions are then explained by the symmetry to which are related. In particular, the way that the various fermions are affected by the different types of interactions is determined by their representations under the corresponding symmetry groups.

Neutrinos are fermions that have neither strong nor electromagnetic interactions. In group theory language, they are singlets of $SU(3)_C \times U(1)_{EM}$.

The Standard Model has three neutrinos. They reside in lepton doublets:

$$L_\ell = \begin{pmatrix} \nu_{L\ell} \\ \ell_L^- \end{pmatrix}, \quad \ell = e, \mu, \tau. \quad (1.4)$$

where e , μ and τ are the charged lepton mass eigenstates. The three neutrino interaction eigenstates, the electron (ν_e), muon (ν_μ) and tau (ν_τ) neutrino, are defined as the states that form the charged currents with their lepton partners, that is, they are the $SU(2)_L$ partners of the charged lepton mass eigenstates (see eq. (1.6)).

The states ν_e , ν_μ and ν_τ are called flavor states, in contrast with the quarks, where flavors are identified with states with a definite mass.

The Lagrangian of the interaction of neutrinos with other particles is given by the Charged Current (CC) and the Neutral Current (NC) Lagrangians:

$$\begin{aligned}
\mathcal{L}_I^{CC} &= -\frac{g}{2\sqrt{2}}j_\alpha^{CC}W^\alpha + \text{h.c.} \\
\mathcal{L}_I^{NC} &= -\frac{g}{\cos\theta_W}j_\alpha^{NC}Z^\alpha
\end{aligned}
\tag{1.5}$$

where g is the electroweak interaction constant, θ_W is the weak angle, W^α and Z^α are the vectorial bosonic fields W^\pm and Z^0 , and j_α^{CC} , j_α^{NC} are the charged and neutral currents of the leptons respectively:

$$\begin{aligned}
j_\alpha^{CC} &= \sum_{\ell=e,\mu,\tau} \bar{\nu}_\ell \gamma_\alpha (1 - \gamma_5) \ell \\
j_\alpha^{NC} &= \sum_{\ell=e,\mu,\tau} \bar{\nu}_\ell \gamma_\alpha (1 - \gamma_5) \nu_\ell
\end{aligned}
\tag{1.6}$$

Why three?

The three flavors of neutrinos seem to be intimately related to the three flavors of leptons and quarks. Nature seems to repeat itself three times with different masses. The reason is not known, but might be a consequence of a symmetry of a higher theory.

There might be other types of neutrinos, but either they don't have any interaction at all (*sterile neutrinos*) or they are very massive. We know that because the number of light (that is, $m_\nu \lesssim m_Z/2$) neutrino flavors have been measured by LEP based on a fit to the Z mass curve. The $Z \rightarrow \nu\bar{\nu}$ channel contributes to the invisible width of the Z decay: $\Gamma_{inv} = \Gamma_{tot} - \Gamma_l - \Gamma_h$, where Γ_{tot} , Γ_l , Γ_h are the total, leptonic (charged) and hadronic widths respectively. The effective number of neutrino species is defined as $N_\nu = \Gamma_{inv}/\Gamma_\nu$, where Γ_ν is the width of the neutrino in the Standard Model. The fit (Fig. 1.9) gives $N_\nu = 2.987 \pm 0.012$, consistent with the expected 3.

1.3.2 Dirac and Majorana

It was Dirac's equation that first led to the concept of particles and antiparticles, the positive electron being the earliest candidate for an antiparticle. While positive electrons are clearly distinct from negative electrons by their electromagnetic properties, it is not obvious in what way neutral particles should differ from their antiparticles. The neutral pion, for example, was found to be identical to its antiparticle. The neutral kaon, on the other hand, is clearly different from its antiparticle.

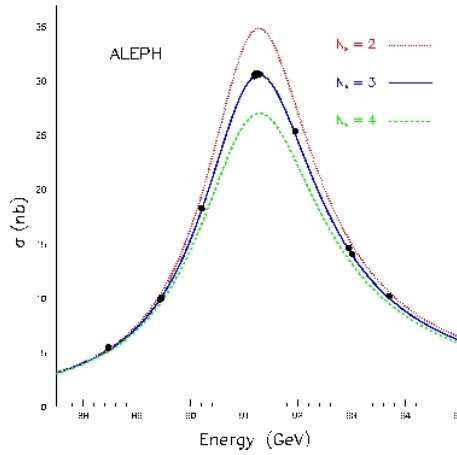


Fig. 1.9: ALEPH 1993: Hadronic cross section as function of c.m. energy. Expectations for 2, 3 and 4 neutrinos are superimposed.

The pion and kaon, both bosons, are not truly elementary particles, however, as they are composed of two charged fermions, the quarks and the antiquarks.

The concept of a particle that is identical to its antiparticle was formally introduced by Majorana in 1937. Thus, such particles are normally referred as Majorana particles. In contrast, what is called a Dirac particle is one which is distinct from its antiparticle.

1.3.3 Neutrino Mass

There was never a good reason for neutrinos not to have mass, because there is not an exact gauge symmetry that forbids them to have it. For photons and gluons, it is the exact symmetries $U(1)$ and $SU(3)$ of the Standard Model the ones that make them have null mass. There is not a gauge boson of null mass corresponding to the leptonic number, and so it was expected to find a non-zero mass to neutrinos.

There are many models of neutrino mass based on GUTs, flavor theories with an additional symmetry $U(1)$ of generation, and recently extra-dimension models. It can be said that neutrino masses allow to foresee physics at a higher scale, possibly further away from the capacity of the experiments with colliders, providing us with an insight at GUTs, flavor physics, and maybe even quantum gravity.

The electroweak Standard Model only has a left neutrino for each generation. That is why the neutrino in this model cannot have a Dirac mass term, as this requires the two helicity states for each particle. However, there is an alternative mass term, called the Majorana mass term, that has not this problem. This term

requires a single state of helicity for the particle and the opposite helicity state for the antiparticle. But it violates the total lepton number in two units and the Standard Model preserves the leptonic number for each generation. Because of that, none of the possible mass terms can appear to any order in a perturbative theory or in presence of non-perturbative effects. As a consequence, in this context there is no neutrino mass, nor neutrino magnetic moment. Detection of neutrino masses is a sign of physics beyond the Standard Model.

1.3.4 Mixing

The main idea in the theory of neutrino oscillations is the fact that neutrinos produced in weak interactions, which are weak interaction eigenstates, are not eigenstates of the mass matrix, which determines how the state of a neutrino evolves in time. Similarly, in the detection process, the neutrino is a weak eigenstate. So, when a neutrino of a given flavor is produced with a definite momentum the different mass states will propagate through space at different velocities. After a while the mass eigenstates will become out of phase with each other, so that the mixture they form will change with time. Hence, what started as a pure muon neutrino becomes a time-varying superposition of all three neutrinos.

2-family Mixing

To illustrate the dynamics of neutrino oscillation, let's consider a 2-flavor neutrino mixing. The flavor eigenstates, ν_e and ν_μ , which are orthogonal, can be written as a linear combination of the mass eigenstates (also orthogonal), ν_1 and ν_2 :

$$\begin{pmatrix} \nu_e \\ \nu_\mu \end{pmatrix} = \begin{pmatrix} \cos \theta & \sin \theta \\ -\sin \theta & \cos \theta \end{pmatrix} \begin{pmatrix} \nu_1 \\ \nu_2 \end{pmatrix} \quad (1.7)$$

that is, using the notation $|\nu\rangle$ to represent the wavefunction vector of the neutrino,

$$\begin{aligned} |\nu_e\rangle &= \cos \theta |\nu_1\rangle + \sin \theta |\nu_2\rangle \\ |\nu_\mu\rangle &= -\sin \theta |\nu_1\rangle + \cos \theta |\nu_2\rangle \end{aligned} \quad (1.8)$$

The mass eigenstates evolve in a very simple way in time, because they are eigenstates of the Hamiltonian:

$$\begin{aligned} |\nu_1(t)\rangle &= e^{-iE_1 t} |\nu_1\rangle = e^{-i\sqrt{m_1^2 + p^2} t} |\nu_1\rangle \\ &\simeq e^{-i(p + \frac{m_1^2}{2p}) t} |\nu_1\rangle \end{aligned}$$

$$|\nu_2(t)\rangle \simeq e^{-i(p + \frac{m_2^2}{2p})t} |\nu_2\rangle \quad (1.9)$$

the approximation being valid for $p \gg m$.

If at $t = 0$ a ν_e is created, its wavefunction will be $|\Psi(0)\rangle = |\nu_e\rangle$, and

$$\begin{aligned} |\Psi(t)\rangle &= c |\nu_1(t)\rangle + s |\nu_2(t)\rangle \\ &\simeq e^{-ip} \left(c e^{-i\frac{m_1^2}{2p}t} |\nu_1\rangle + s e^{-i\frac{m_2^2}{2p}t} |\nu_2\rangle \right) \end{aligned} \quad (1.10)$$

where $c \equiv \cos \theta$ and $s \equiv \sin \theta$ to simplify the notation.

The probability that the original $|\nu_e\rangle$, now $|\Psi(t)\rangle$, has oscillated to a $|\nu_\mu\rangle$ is

$$\begin{aligned} P_{\nu_e \rightarrow \nu_\mu}(t) &= |\langle \nu_\mu | \Psi(t) \rangle|^2 \\ &\simeq \left| (-s \langle \nu_1 | + c \langle \nu_2 |) \left(c e^{-i\frac{m_1^2}{2p}t} |\nu_1\rangle + s e^{-i\frac{m_2^2}{2p}t} |\nu_2\rangle \right) \right|^2 \\ &= \left| -sc e^{-i\frac{m_1^2}{2p}t} + cs e^{-i\frac{m_2^2}{2p}t} \right|^2 \\ &= 2s^2 c^2 \left(1 - \cos \left(\frac{m_2^2 - m_1^2}{2p} t \right) \right) \\ &= \sin^2(2\theta) \sin^2 \left(\frac{\Delta m^2}{4p} t \right) \\ &\simeq \sin^2(2\theta) \sin^2 \left(\frac{\Delta m^2}{4E} L \right) \end{aligned} \quad (1.11)$$

where $\Delta m^2 \equiv m_2^2 - m_1^2$ and we have used $\cos^2(x) \sin^2(x) = \frac{1}{4} \sin^2(2x)$, $1 - \cos(2x) = 2 \sin^2 x$, and, in natural units, $p \simeq E$, $t \simeq L$, where L is the distance at which we detect the neutrino.

The oscillation probability is a periodic function of the distance. As we can see in (1.11), the maximum oscillation happens for $\theta = \pi/4$, that is, maximal mixing between flavor and mass eigenstates, and the period of the oscillation is $2\pi \frac{2E}{\Delta m^2}$.

3-family Mixing

The current atmospheric and solar neutrino data can be easily accommodated in a three-family mixing scenario. If we write the weak eigenstates as a function of the mass eigenstates (see Fig. 1.10) we get the leptonic equivalent of the Cabibbo-Kobayashi-Maskawa matrix, the Pontecorvo-Maki-Nakagawa-Sakata (PMNS) matrix:

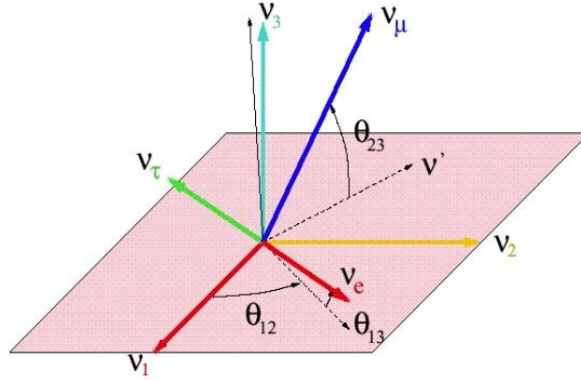


Fig. 1.10: Mixing of the three flavor eigenstates with the three mass eigenstates.

$$\begin{pmatrix} \nu_e \\ \nu_\mu \\ \nu_\tau \end{pmatrix} = U \begin{pmatrix} \nu_1 \\ \nu_2 \\ \nu_3 \end{pmatrix} \quad (1.12)$$

$$\begin{aligned} U &\equiv U_{23}U_{13}U_{12} \quad (1.13) \\ &\equiv \begin{pmatrix} 1 & 0 & 0 \\ 0 & c_{23} & s_{23} \\ 0 & -s_{23} & c_{23} \end{pmatrix} \begin{pmatrix} c_{13} & 0 & s_{13}e^{i\delta} \\ 0 & 1 & 0 \\ -s_{13}e^{-i\delta} & 0 & c_{13} \end{pmatrix} \begin{pmatrix} c_{12} & s_{12} & 0 \\ -s_{12} & c_{12} & 0 \\ 0 & 0 & 1 \end{pmatrix} \end{aligned}$$

with $c_{ij} \equiv \cos \theta_{ij}$ and $s_{ij} \equiv \sin \theta_{ij}$. There are three mixing angles θ_{ij} and one phase δ , that if different from zero, would be responsible of CP violation.

This decomposition parameterizes the 3D rotation matrix as the product of three independent rotations, one in the plane 23 (which will be responsible for the atmospheric transitions), another in the plane 12 (solar transitions) and a third one that connects both.

Without loss of generality we can choose the convention in which all Euler angles lie in the first quadrant, $0 \leq \theta_{ij} \leq \pi/2$, while the CP-phase is unrestricted, $0 \leq \delta < 2\pi$.

The transition probabilities between different flavors are

$$P(\nu_\alpha \rightsquigarrow \nu_\beta) = -4 \sum_{k>j} \text{Re}[W_{\alpha\beta}^{jk}] \sin^2 \left(\frac{\Delta_{jk}L}{2} \right) \pm 2 \sum_{k>j} \text{Im}[W_{\alpha\beta}^{jk}] \sin^2(\Delta_{jk}L) \quad (1.14)$$

where $W_{\alpha\beta}^{jk} \equiv [U_{\alpha j} U_{\beta j}^* U_{\alpha k}^* U_{\beta k}]$ and $\Delta_{jk} \equiv \frac{\Delta m_{jk}^2}{2E_\nu}$, with the plus and minus sign referring to neutrinos and antineutrinos respectively.

With the currently known $\Delta m_{12}^2 \ll \Delta m_{23}^2$ and $\sin^2 2\theta_{13} \ll 1$, it is possible to derive approximate expressions that can help to understand the behaviour of the probability. They will be presented in the next chapters. The main remark here is that the oscillation probabilities in three neutrino families are described by two mass differences (Δm_{12}^2 and Δm_{23}^2) and 4 parameters from the PMNS matrix: three mixing angles (θ_{12} , θ_{23} , θ_{13}) and a phase (δ). The presence of this phase in the mixing matrix makes it possible to study CP violation, and is commonly called the *CP-violating phase*.

1.3.5 Matter Effects

Wolfenstein pointed out that the patterns of neutrino oscillation might be significantly affected if the neutrinos travel through a material medium rather than through the vacuum. The basic reason for this is simple. Normal matter has electrons but no muons or taus at all. Thus, if a ν_e beam goes through matter, it encounters both charged and neutral current interactions with the electrons. But a ν_μ or a ν_τ interacts with the electron only via the neutral current, so their interaction is different in magnitude than that of the ν_e .

Interactions modify the effective mass that a particle exhibits while travelling through a medium. A well-known example is that of the photon, which is massless in the vacuum but develops an effective mass in a medium. As a result, electromagnetic waves do not travel with speed c through a medium. The effective masses of neutrinos are similarly modified in a medium by their interactions. Since ν_e has a different interaction than the other neutrinos, the modification is different for ν_e than for the other flavored neutrinos.

This fact can have dramatic consequences if the neutrinos mix in the vacuum. In this case, a physical eigenstate can have components of ν_e , ν_μ , ν_τ and other possible states. When such a state travels through a medium, the modulation of its ν_e component is different from the same modulation inside the vacuum. This leads to changes in the oscillation probabilities compared to their values in the vacuum.

We will see an example in a simplified case with only ν_e and ν_μ , and assume that the density of the background matter is uniform, with n_e , n_p and n_n denoting the number of electrons, protons and neutrons per unit volume. Elastic scattering of these particles changes the effective masses of the neutrinos.

Elastic scattering through charged current interactions can only happen between ν_e and e . The effective lagrangian for such an interaction is:

$$\begin{aligned} & \frac{4G_F}{\sqrt{2}} (\bar{e}(p_1)\gamma_\lambda P_L \nu_e(p_2)) (\bar{\nu}_e(p_3)\gamma^\lambda P_L e(p_4)) \\ & \frac{4G_F}{\sqrt{2}} (\bar{\nu}_e(p_3)\gamma_\lambda P_L \nu_e(p_2)) (\bar{e}(p_1)\gamma^\lambda P_L e(p_4)) \end{aligned} \quad (1.15)$$

where the second form is obtained via Fierz transformation. For forward scattering where $p_2 = p_3 = p$, this gives the following contribution that affects the propagation of the ν_e :

$$\sqrt{2}G_F \bar{\nu}_{eL}(p)\gamma_\lambda \nu_{eL}(p) \langle \bar{e}\gamma^\lambda(1 - \gamma_5)e \rangle \quad (1.16)$$

averaging the electron field bilinear over the background. To calculate that average, using that the axial current reduces to spin in the non-relativistic approximation, which is negligible for a non-relativistic collection of electrons. The spatial components of the vector current give the average velocity, which is negligible as well. So the only non-trivial average is

$$\langle \bar{e}\gamma^0 e \rangle = \langle e^\dagger e \rangle = n_e \quad (1.17)$$

which gives a contribution to the effective lagrangian

$$\sqrt{2}G_F n_e \bar{\nu}_{eL}\gamma_0 \nu_{eL} \quad (1.18)$$

This effectively adds an amount $\sqrt{2}G_F n_e$ to the energy of the particle.

For neutral current contributions, we can find in the same way the following contributions to effective energies of both ν_e and ν_μ :

$$\sqrt{2}G_F \sum_f n_f \left(I_{3L}^{(f)} - 2 \sin^2 \theta_W Q^{(f)} \right) \quad (1.19)$$

where f stands for the electron, the proton or the neutron, $Q^{(f)}$ is the charge of f and $I_{3L}^{(f)}$ is the third component of weak isospin of the left-chiral projection of f . Thus, for the proton, $Q = 1$ and $I_{3L} = -1/2$, whereas for the electron, $Q = -1$ and $I_{3L} = -1/2$. Also, for normal neutral matter, $n_e = n_p$ to guarantee charge neutrality. Therefore the contributions of the electron and the proton cancel each other and we are left with the neutron contribution, which is

$$-\sqrt{2}G_F n_n / 2 \quad (1.20)$$

This neutral current is *the same for all flavors of neutrinos*, while the charged current contribution affects ν_e only. Thus, in the evolution equation of neutrino beams:

$$\frac{d}{dt} \begin{pmatrix} \nu_e \\ \nu_\mu \end{pmatrix} = H_{flavor} \begin{pmatrix} \nu_e \\ \nu_\mu \end{pmatrix} \quad (1.21)$$

where $H_{flavor} = UHU^\dagger$, H' is replaced by

$$H'' = H' - \frac{1}{\sqrt{2}}G_F n_n + \begin{pmatrix} \sqrt{2}G_F n_e & 0 \\ 0 & 0 \end{pmatrix} \quad (1.22)$$

The effective mixing angle in matter, $\tilde{\theta}$, would accordingly be given by

$$\tan 2\tilde{\theta} = \frac{2H'_{12}}{H'_{22} - H'_{11}} = \frac{(m_2^2 - m_1^2) \sin 2\theta}{(m_2^2 - m_1^2) \cos 2\theta - A} \quad (1.23)$$

where $A = 2\sqrt{2}G_F n_e E$.

The effective mixing angle thus changes inside matter. The change is most dramatic if $A = (m_2^2 - m_1^2) \cos 2\theta$, that is, if the electron number density is given by:

$$n_e = \frac{(m_2^2 - m_1^2) \cos 2\theta}{2\sqrt{2}G_F E} \quad (1.24)$$

Then, even if the vacuum mixing angle θ is small, we have $\tilde{\theta} = \pi/4$, which is to say that ν_e and ν_μ mix maximally. This phenomenon is known as *resonance*.

2. MEASURING THE MIXING PARAMETERS AND MASSES

2.1 Main experimental lines

The 4 parameters in the PMNS matrix are more or less separately measured by different types of experiments:

$$\underbrace{\begin{pmatrix} 1 & 0 & 0 \\ 0 & c_{23} & s_{23} \\ 0 & -s_{23} & c_{23} \end{pmatrix}}_{\substack{\text{Atmospheric,} \\ \text{1st generation of} \\ \text{Long Baseline} \\ \text{Experiments}}} \underbrace{\begin{pmatrix} c_{13} & 0 & s_{13}e^{i\delta} \\ 0 & 1 & 0 \\ -s_{13}e^{-i\delta} & 0 & c_{13} \end{pmatrix}}_{\substack{\text{2nd generation of} \\ \text{Long Baseline} \\ \text{Experiments}}} \underbrace{\begin{pmatrix} c_{12} & s_{12} & 0 \\ -s_{12} & c_{12} & 0 \\ 0 & 0 & 1 \end{pmatrix}}_{\substack{\text{Solar and Reactor} \\ \text{Experiments}}} \quad (2.1)$$

We can classify the experiments in many different categories depending on:

- Neutrino Source
 - Sun
 - Cosmic Rays
 - Laboratory Beams
 - * Accelerator
 - * Reactor
- Type
 - Appearance ($\nu_X \rightsquigarrow \nu_Y$)
 - Disappearance ($\nu_X \rightsquigarrow \nu_X$)
- Distance
 - Short ($\lesssim 1$ km) baseline
 - Long baseline

This is a brief survey of the main neutrino experiments that have been done in the past, are currently working, or are in an advanced development stage:

- Neutrino experiments at particle accelerators (including long-baseline neutrino beams)
 - BooNE [Booster Neutrino Experiment]: planned experiment at Fermilab
 - CHORUS [CERN Hybrid Oscillation Research apparatus]: experiment at CERN
 - COSMOS [COsmologically Significant Mass Oscillation Search]: Experiment E803 at FermiLab
 - KARMEN [KARlsruhe Rutherford Intermediate Energy Neutrino Experiment]
 - KEK-PS E362 (K2K: KEK to Kamioka) New long-baseline neutrino oscillation experiment from KEK PS to Super-Kamiokande
 - LSND [Liquid Scintillator Neutrino Detector] at Los Alamos
 - MINOS [Main Injector Neutrino Oscillation Search] Future experiment with neutrino beam from FNAL to Sudan.
 - NOE [Neutrino Oscillation Experiment]: planned CERN to Gran Sasso long-baseline experiment.
 - NOMAD [Neutrino Oscillation MAgnetic Detector] experiment at CERN.
 - NuTeV (Fermilab experiment E815, measures mainly $\sin^2\theta_{23}$).
 - OPERA [Oscillation Project with Emulsion-tRacking Apparatus]: proposed CERN to Gran Sasso long-baseline experiment.
 - TAU (Fermilab experiment E 872)
 - TOSCA [Topological Oscillation Search with kinematiCal Analysis]: intended CERN short-baseline experiment.
- Neutrino experiments at reactors
 - CHOOZ (reactor neutrino oscillations experiment, Ardennes, France)
 - KamLAND (in the Kamioka mine, Japan).
 - MUNU (at the Bugey nuclear power plant, France).
 - Palo Verde neutrino oscillation experiment.
- Underground experiments

-
- BOREXINO experiment at Gran Sasso.
 - CERN underground muon experiments Cosmics with L3 and CosmoLEP
 - GALLEX [GALLium EXperiment] a former solar neutrino experiment at Gran Sasso
 - GNO [Gallium Neutrino Observatory] is the successor project of GALLEX
 - Various GRAN SASSO experiments [GALLEX, LVD, MACRO, and others]
 - HELLAZ [HELIum à la température de L'AZote liquide] (proposed solar neutrino detector).
 - HERON R and D project
 - Homestake chlorine experiment.
 - ICARUS [Imaging Cosmic And Rare Underground Signal]: Liquid argon TPC detector to be build at Gran Sasso.
 - IMB [Irvine Michigan Brookhaven] experiment
 - LVD experiment [Large Volume Detector] at Gran Sasso.
 - MACRO [Monopole, Astrophysics, Cosmic Rays] (see also pages prepared by Boston, Caltech, Texas A and M, and Pisa participants).
 - OMNIS [Observatory for Multiflavor NeutrInos from Supernovae]
 - SAGE [Soviet-American Gallium Experiment]
 - SNO [Sudbury Neutrino Observatory]
 - SOUDAN-2 (Tower-Soudan Iron Mine, Minnesota, USA)
 - Super Kamiokando (S-K)
- Underwater experiments
 - ANTARES [Astronomy with a Neutrino Telescope and Abyss environmental RESearch]
 - Baikal (underwater neutrino experiment in Lake Baikal, Russia).
 - DUMAND [Deep Undersea Muon and Neutrino Detector], prepared by Univ. of Washington participants.
 - NEMO [NEutrino subMARine Observatory] (apparently in early planning phase)
 - Experiments in Antarctic ice (at the South Pole)
 - AMANDA [Antarctic Muon and Neutrino Detector].

- ICECUBE (a planned kilometer-scale neutrino observatory)
- RAND [Radio Array Neutrino Detector]
- RICE [Radio Ice Cerenkov Experiment]

2.2 Reactor Experiments

Reactor experiments are disappearance experiments looking for $\bar{\nu}_e \rightarrow \bar{\nu}_X$. Reactors are a source of $\bar{\nu}_e$ of a few MeV, due to the fission products being β -unstable. Experiments typically try to measure the positron spectrum, which can be deduced from the $\bar{\nu}_e$ spectrum, and either compare it directly to the theoretical predictions or measure it at several distances from the reactor and search for spectral changes. Both types of experiments were done in the past. The reaction is



with an energy threshold of 1.804 MeV. Coincidence techniques are used between the annihilation photons and the neutrons which diffuse and thermalize within 10-100 μs . The main background are cosmic ray muons producing neutrons in the surrounding of the detector.

Some examples from the already finished reactor experiments are Bugey, Savannah, Rovno and Krasnojarsk. In all of them the main detector has a mass $\lesssim 0.5$ ton and the distances are $\lesssim 250$ m.

Nowadays, the main reactor experiments are CHOOZ, Palo Verde and KamLAND. They have much higher masses than the older experiments (1 kton for KamLAND). CHOOZ is located underground to reduce the contamination produced by cosmic rays. This experiment gives a limit for the mixing angle θ_{13} , the key element for the connection between solar and atmospheric neutrinos: $\sin^2 2\theta_{13} < 0.15$.

The KamLAND experiment, installed in the Kamioka mine in Japan (see Fig. 2.1), has recently published its first results [13]. It uses measurements at large distances ($\simeq 180$ km) and it is then very sensitive to a small Δm^2 . It is the first reactor experiment to establish $\bar{\nu}_e$ disappearance at a high confidence level (99.95%). It has 1 kton of liquid scintillator as main target, filled in a plastic balloon. There are 6 reactors with a total thermal power of 69 GW in a distance between 140 and 210 km to Kamioka, which produce a total neutrino flux of $1 \times 10^6/cm^2/s$ at Kamioka for $\bar{\nu}_e$ energies larger than 1.8 MeV, resulting in 2 events/day.

Originally proposed for solar neutrino detection, also the BOREXINO experiment has the ability to investigate reactor neutrinos. The $\bar{\nu}_e$ flux at Gran Sasso is around $1.5 \times 10^5/cm^2/s$ for energies larger than 1.8 MeV produced by power plants ~ 800 km away. Without oscillation, this would result in 27 events/year.

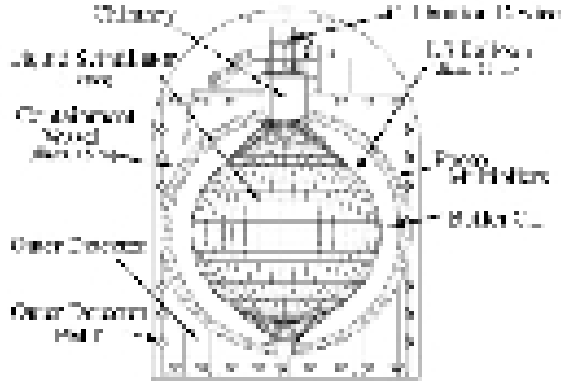


Fig. 2.1: Schematic of the KamLAND detector.

2.3 Accelerator Experiments

The long baseline accelerator experiments focus on the investigation of the atmospheric neutrino anomaly. Typical neutrino beams at accelerators are produced by protons hitting a fixed target, where the decaying secondaries (mostly pions) decay into ν_μ . This dominantly ν_μ beams are then used wither for pure ν_μ disappearance searches or for appearance searches by measuring electrons and/or taus produced by charged current interactions.

2.3.1 K2K

The first of the accelerator based long baseline experiments is the KEK-E362 experiment (K2K) in Japan sending a neutrino beam from KEK to Super-Kamiokande (see Fig. 2.2). It is using two detectors, one at about 300 m away from the target, and Super-Kamiokande in a distance of about 250 km. The neutrino beam is produced by 12 GeV protons from the KEK-PS hitting an Al target.

An almost pure ν_μ beam is produced by selecting π^+ with a magnetic horn and letting them decay in a tunnel of 200 m. The contamination of ν_e from μ and K decay is of the order 1%. The protons are extracted in a fast extraction mode allowing spills of a time width of 1.1 μs every 2.2 seconds. With 6×10^{12} protons on target (pots) per spill, about 10^{20} pots can be accumulated in 3 years. The average neutrino beam energy is 1.3 GeV, with a peak at about 1 GeV.

The near detector consists of two parts, a 1 kton water Cerenkov detector and



Fig. 2.2: The K2K experiment.

a fine grained detector. The water detector's main goal is to allow a direct comparison with Super-Kamiokande events and to study systematic effects of this detection technique. The fine grained detector basically consists of four parts and should provide information on the neutrino beam profile as well as the energy distribution. First of all there are 20 layers of scintillating fiber trackers intersected with water. The position resolution of the fiber sheets is about $280 \mu\text{m}$ and allows track reconstruction of charged particles and therefore the determination of the kinematics in the neutrino interaction. In addition to trigger counters there is a lead-glass counter and a muon detector. The 600 lead glass counters are used for measuring electrons and therefore to determine the ν_e beam contamination. The energy resolution is about $8\%/\sqrt{E}$. The muon chambers consist of 900 drift tubes and 12 iron plates. Muons generated in the water target via charged current reactions can be reconstructed with a position resolution of 2.2 mm. The detection method within Super-Kamiokande is identical to that of their atmospheric neutrino detection. Precise timing cuts with the beam pulse are applied.

The low beam energy allows K2K only to perform a search for $\nu_\mu \rightsquigarrow \nu_e$ appearance and a ν_μ disappearance. The main background for the search in the electron channel is quasielastic π^0 production in neutral current reactions.

The sensitivity regions are $\Delta m_{23}^2 > 2 \times 10^{-3} \text{eV}^2$ and $\sin^2 2\theta_{13} > 0.1$ for $\nu_\mu \rightsquigarrow \nu_e$, not completely covering the atmospheric parameters.

2.3.2 NuMI

A neutrino program is also associated with the new main injector at Fermilab. The long baseline project will send a neutrino beam produced by 120 GeV protons to the Soudan mine about 730 km away from Fermilab. Here the MINOS experiment is under construction. It consists of a 980 ton near detector located at Fermilab about 900 m away from a graphite target and a far detector at Soudan. The far detector will be made of 486 magnetized iron plates, producing an average toroidal magnetic field of 1.5 T. They have a thickness of 2.54 cm and an octagonal shape measuring 8 m across. They are interrupted by about 25800 m^2 active detector planes in form of 4.1 cm wide solid scintillator strips with x and y readout to get the necessary tracking informations. Muons are identified as tracks transversing at least 5 steel plates, with a small number of hits per plane. The total mass of the detector will be 5.4 ktons. The neutrino beam energy can be tuned by positioning the magnetic horn system in various positions relative to the target, resulting in different beam energies.

Oscillation searches in the $\nu_\mu \rightsquigarrow \nu_e$ and $\nu_\mu \rightsquigarrow \nu_\tau$ channel can be done in several ways. ν_μ disappearance searches can be performed by investigating the visible energy distributions in charged current events. A powerful way to search for oscillations is to compare the NC/CC ratio in the near and far detectors. In three years exposure it will cover the full atmospheric region. Start data taking is foreseen around 2005.

2.3.3 CNGS

CERN has been engaged in a somewhat controversial experiment to send a neutrino beam to Gran Sasso (CNGS). The distance is 732 km. The beam protons from the SPS can be extracted with energies up to 400 GeV hitting a graphite target in a distance of 830 m to the SPS. A magnetic horn system will select the pions that will decay in a 1 km tunnel. The average energy is around 20 GeV, optimized for ν_τ appearance searches.

Two experiments are under consideration for the Gran Sasso Laboratory to perform an oscillation search. The first proposal is the ICARUS experiment. This liquid Ar TPC with a modular design ideally offers excellent energy and position resolution. Beside a ν_μ disappearance search by looking for a distortion in the energy spectra, also a ν_e appearance search can be done because of the good electron identification capabilities. A ν_τ appearance search will be performed by using kinematical criteria as in NOMAD.

The second proposal is a ν_τ appearance search with a 2 kton lead-emulsion sandwich detector, OPERA. The idea is to use a combination of 1 mm lead plates

as a massive target for neutrino interactions and two thin ($50 \mu\text{m}$) emulsion sheets separated by $200 \mu\text{m}$, conceptually working as emulsion cloud chambers. The detector has a modular design, with a brick containing 56 Pb/emulsion sheets as basic building block. 3264 bricks together with electronic trackers form a module. 24 modules will form a supermodule of about 652 ton. Three supermodules interleaved with a muon spectrometer finally form the full detector. The scanning of the emulsions is done by high speed automatic CCD microscopes. The tau, produced by CC reactions in the lead, can be investigated by two signatures. For long decays the emulsion sheets are used to verify the kink of the τ decay, while for short decays an impact parameter analysis can be performed identifying tracks not pointing towards the primary vertex point. The analysis here is done on an event per event basis. In five years of data taking, a total of 18 events are expected.

2.4 Status as 2003

In 1998 the Super-Kamiokande data, presenting an up-down asymmetry of high energy events generated by atmospheric ν_μ , provided a model independent proof for atmospheric ν_μ disappearance. They are interpreted as oscillations of muon neutrinos into neutrinos that are not ν_e 's, with a mass gap Δm_{23}^2 . Roughly speaking, the measured mixing angle θ_{23} is close to maximal and $|\Delta m_{23}^2|$ is in the range $10^{-3} - 10^{-2} eV^2$.

About one year ago, the observation of solar neutrinos through neutral and charged current reactions allowed the SNO experiment to solve the long-standing solar neutrino problem in favor of the existence of $\nu_e \rightsquigarrow \nu_\mu, \nu_\tau$ oscillations. The global analysis of all solar neutrino data in terms of the most natural hypothesis of neutrino oscillations favored the Large Mixing Angle (LMA) region with $2 \times 10^{-5} eV^2 \lesssim \Delta m_{12}^2 \lesssim 4 \times 10^{-4} eV^2$ and a large effective mixing angle $0.2 \lesssim \tan \theta_{12} \lesssim 0.9$. A spectacular proof of the correctness of the LMA region has been obtained at the end of last year in the KamLAND $\bar{\nu}_e$ disappearance experiment, in which a suppression of $0.611 \pm 0.085 \pm 0.041$ of the $\bar{\nu}_e$ flux was observed. The allowed regions of the effective neutrino oscillation parameters obtained from the global analysis of solar and KamLAND neutrino data can be seen in Fig. 2.3. Transitions of solar ν_e into sterile states are also disfavored by the data.

In the future it is expected that the KamLAND experiment will allow to distinguish between the LMA-I and LMA-II regions, reaching a relatively high accuracy in the determination of Δm_{12}^2 . Last September 7, SNO published the result from their salt run with an enhanced sensitivity to the NC process [14]. The new result agrees well with previous results, confirming the LMA solution. In addition they have reported a much better determination of the mixing angle θ_{12} , which excludes

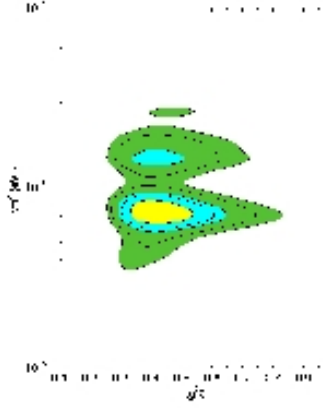


Fig. 2.3: Allowed 1 to 4 σ C. L. regions obtained from the global analysis of solar and KamLAND data.

the maximal mixing $\theta_{12} = \pi/4$ at 5.4σ .

At the end of 2002 the long baseline K2K experiment confirmed the neutrino oscillation interpretation of the atmospheric neutrino anomaly observing the disappearance of accelerator ν_μ 's. The data of atmospheric and K2K experiments are well fitted by $\nu_\mu \rightsquigarrow \nu_\tau$ transitions generated by Δm_{23}^2 in the 99.73% C. L. range: $1.4 \times 10^{-3} eV^2 < \Delta m_{23}^2 < 5.1 \times 10^{-3}$, with best-fit value $\Delta m_{23}^2 \simeq 2.6 \times 10^{-3} eV^2$.

The solar and atmospheric evidences of neutrino oscillations are nicely accommodated in the minimal framework of three neutrino mixing. In the case of three-neutrino mixing there are no sterile neutrinos, in agreement with the absence of any indication in favor of active-sterile transitions in both solar and atmospheric neutrino experiments. However, the three neutrino mixing scenario does not accommodate the short baseline $\bar{\nu}_\mu \rightsquigarrow \bar{\nu}_e$ transitions observed in the LSND experiment, which are presently under investigation in the MiniBooNE experiment.

The negative results of the CHOOZ long baseline $\bar{\nu}_e$ disappearance experiment implies that electron neutrinos do not oscillate at the atmospheric scale. This sets the limit in the mixing angle that connects the atmospheric and solar oscillations in $\sin^2 2\theta_{13} < 0.11$.

In conclusion, the recent years have been extraordinarily fruitful for neutrino physics, yielding model-independent proof of solar and atmospheric neutrino oscillations, which have provided important information on the neutrino mixing parameters.

The next generation of neutrino experiments will make more precision mea-

measurements of the already known mixing parameters and could also be sensitive to the remaining unknown PMNS parameters, θ_{13} and the CP-violating phase δ .

3. THE ULTIMATE MACHINE: NEUTRINO FACTORY

3.1 *Origin of the Idea*

In a Neutrino Factory, neutrinos are produced by the decays of muons circulating in a storage ring. Most of what is known of muon storage rings is due to the pioneering work of the Muon Collider Collaboration. They were able to formulate and to a large extent simulate the basic concepts of a Muon Collider. The concept of a Neutrino Factory was born from the observation that the beams of neutrinos emitted by the decaying muons along the accelerator chain or in the storage rings could be valuable physics tools [15], the potential of which was emphasized in the ECFA prospective study. The Neutrino Factory design is presently being pursued in the United States, at CERN and in Japan.

3.2 *Characteristics*

The main advantage of neutrino factories over conventional beams is the purity of the beam. In a conventional beam an intense proton beam hits a target, and the produced hadrons are focused and finally let decay in a long tunnel, thus producing an almost pure ν_μ or $\bar{\nu}_\mu$ beam. However, the small background is what makes oscillation experiments difficult. About 1% of ν_e and antineutrinos of both flavors, produced by the three-body decays $K^+ \rightarrow e^+\pi^0\nu_e$ and $K_L \rightarrow e^\pm\pi^\mp\nu_e(\bar{\nu}_e)$, and tertiary muons that decay before they can be absorbed, $\mu^\pm \rightarrow e^\pm\nu_e(\bar{\nu}_e)\bar{\nu}_\mu(\nu_\mu)$.

If one is trying to measure large effects this contamination would not be a big problem, but the next step in neutrino oscillation physics will be to look for an effect which has already been determined by experiment to be less than about 5%. Precisely knowing this intrinsic background and subtracting it from a potential signal will be the only way to make the measurement. Also, to most massive detectors, neutral current events, in which there is no final state muon, can fake the ν_e charged current events.

On the other hand, the beams produced by a neutrino factory (with, for instance, μ^+ in the storage ring), $\mu^+ \rightarrow e^+\nu_e\bar{\nu}_\mu$, gives a mixture of ν_e 's and $\bar{\nu}_\mu$'s, but absolutely no other flavors. The $\bar{\nu}_\mu$'s that do not oscillate will give μ^+ 's at the detector (allowing to count for the disappearance of $\bar{\nu}_\mu$'s), but the ν_e 's can oscillate

to a ν_μ and then give a μ^- at the detector, that is, a “wrong sign muon”. As there are no ν_μ ’s in the beam, then, in the absence of detector backgrounds (which are much smaller than in the conventional case) any observation of μ^- ’s signals the existence of a $\nu_e \rightsquigarrow \nu_\mu$ transition.

The final important fact to note about these measurements is that simply by measuring both $\nu_e \rightsquigarrow \nu_\mu$ and $\bar{\nu}_e \rightsquigarrow \bar{\nu}_\mu$, one can access all of the interesting parameters which describe the neutrino mixing [16]. So, although neutrino factories in principle allow the measurements of all possible transitions between one flavor neutrino to another, one can extract all the interesting physics precisely, by simply building a massive detector that can measure the charge and energy of muons, a well understood detector technology.

A final advantage of muon-induced neutrino beams is that they are very well understood from the theoretical point of view.

The next generation of Super Beams will improve the precision of Δm_{23}^2 and θ_{23} . Nevertheless, with all this conventional neutrino beams there will not be any significant improvement in the knowledge of:

- The angle θ_{13} , which is the key between the atmospheric and solar neutrino realms, for which the present CHOOZ bound is $\theta_{13} < 13^\circ$.
- The sign of Δm_{23}^2 , which determines whether the three-family neutrino spectrum is of the “hierarchical” or “degenerate” type (i.e. only one heavy state and two almost degenerate light ones, or the reverse).
- Leptonic CP-violation.
- The precise study of matter effects in the ν propagation through the Earth: a model-independent experimental confirmation of the MSW effect will not be available.

3.3 *General Design*

The design includes a very high-power proton driver, delivering on target typically 4 MW of beam power of protons with energy in excess of a few GeV. A superconducting linac at 2.2 GeV has been studied at CERN, while the US design calls for a rapid cycling proton synchrotron at 16-24 GeV, and an upgrade of JHF is considered in Japan. Designing a target that can withstand the thermal shock and heat load naturally leads to a liquid jet target design, although rotating high temperature solids are also being considered. Pions produced are collected as efficiently as possible by a magnetic channel, which involves a 20 T solenoid or powerful magnetic

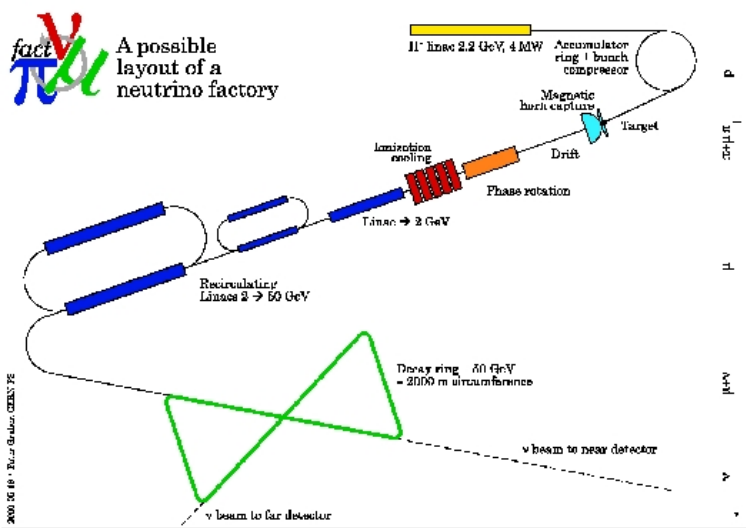


Fig. 3.1: Schematic layout of the CERN scenario for a Neutrino Factory.

horns. Pions quickly decay into muons with a similar energy spectrum. At this point the beam is 0.6 m in diameter and has an energy spread of more than 100%.

A momentum interval near the largest particle density, typically 250 ± 100 MeV, is monochromatized to within a few MeV by means of phase rotation, using a strong variable electric field to slow down the fastest particles and accelerate the slower ones. This requires low-frequency ($\sim 50 - 100$ MHz) RF cavities or an induction linac. To reduce the transverse emittance, cooling is necessary, and is provided by ionization cooling. This involves energy loss of muons through a low-Z material, e. g. , liquid hydrogen, in a strongly focusing magnetic field (solenoids of 5-10 Tesla), which reduces momentum in all three dimensions, followed by accelerating RF cavities, which restore the longitudinal momentum. The net effect is a reduction of emittance, leading to a transverse beam size of a few centimeters.

This leads to a linear configuration, as shown in Fig. 3.1, for the initial muon beam preparation section, or *muon front-end*. In this concept, each beam element is used only once. It could be interesting, to save hardware, to be able to perform phase rotation and/or transverse cooling in a recirculating configuration. Indeed, a system of large aperture FFAG accelerators with low frequency RF (around 1.5 MHz) is the key to the Japanese Neutrino Factory design. Also, much progress has recently been made on ‘ring coolers’, which allow both transverse and longitudinal cooling in a circular configuration.

Assuming that the delicate questions of optics can be solved, these ‘ring’ op-

tions share the difficulty of injecting or extracting from a ring the very large emittance beam of muons available at the end of the decay channel. The possibility of very large aperture and very fast kickers is the major unknown and will be a key issue for these potentially cost-saving developments.

Finally, a linac followed by recirculating linacs - or FFAG accelerators - provide the fast acceleration of muons to an energy of 20 to 50 GeV. Around 10^{21} muons per year of 10^7 seconds could then be stored in a ring, where they would circulate for a few hundred times during their lifetime. The storage ring can take the shape of a racetrack, triangle or bow-tie. These latter two configurations allow several beams of decay neutrinos to be produced in the direction of short- and long-baseline experiments. Optics have been designed for muon storage rings of either triangular or bow-tie geometry, pointing for instance at distances of 730 km (which would correspond to the CERN-Gran Sasso beam line), and 2800 km (which would correspond to a more distant site in the Canary Islands or the Nordic countries).

Neutrino Factory design involves many new components and extrapolations beyond state-of-the-art technology. The first design studies have come to the conclusion that, with the present designs and technology, such a machine could indeed be built and reach the desired performance, but that various work was needed to bring the cost down. Assuming adequate funding, it is considered that about five years of research and development will be necessary to reach a point where a specific, cost-evaluated machine can be proposed.

3.4 Muon Beams, Fluxes and Rates

In the muon rest-frame, the distribution of $\bar{\nu}_\mu(\nu_\mu)$ and $\nu_e(\bar{\nu}_e)$ in the decay $\mu^\pm \rightarrow e^\pm \nu_e(\bar{\nu}_e) \bar{\nu}_\mu(\nu_\mu)$ is

$$\frac{d^2 N}{dx d\Omega} = \frac{1}{4\pi} (f_0(x) \mp \mathcal{P}_\mu f_1(x) \cos \theta) \quad (3.1)$$

where $x = 2E_\nu/m_\mu$, \mathcal{P}_μ is the average muon polarization along the beam direction and θ is the angle between the neutrino momentum vector and the muon spin direction. The functions f_0 and f_1 are given in Table 3.1.

	$f_0(x)$	$f_1(x)$
ν_μ, e	$2x^2(3 - 2x)$	$2x^2(1 - 2x)$
ν_e	$12x^2(1 - x)$	$12x^2(1 - x)$

Tab. 3.1: Flux functions in the muon rest-frame.

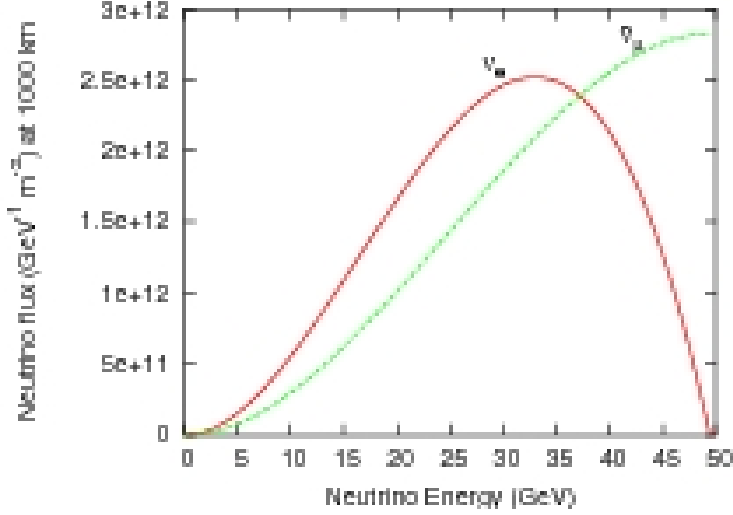


Fig. 3.2: Energy distribution of a neutrino beam from the decay $\mu^+ \rightarrow e^+ \nu_e \bar{\nu}_\mu$.

In the laboratory frame, the neutrino fluxes, boosted along the muon momentum vector, are given by

$$\begin{aligned}
 \frac{d^2 N_{\bar{\nu}_\mu, \nu_\mu}}{dy dS} &= \frac{4n_\mu}{\pi L^2 m_\mu^6} E_\mu^4 y^2 (1 - \beta \cos \phi) \left\{ (3m_\mu^2 - 4E_\mu^2 y (1 - \beta \cos \phi)) \right. \\
 &\quad \left. \mp \mathcal{P}_\mu (m_\mu^2 - 4E_\mu^2 y (1 - \beta \cos \phi)) \right\} \\
 \frac{d^2 N_{\nu_e, \bar{\nu}_e}}{dy dS} &= \frac{24n_\mu}{\pi L^2 m_\mu^6} E_\mu^4 y^2 (1 - \beta \cos \phi) \left\{ (m_\mu^2 - 2E_\mu^2 y (1 - \beta \cos \phi)) \right. \\
 &\quad \left. \mp \mathcal{P}_\mu (m_\mu^2 - 2E_\mu^2 y (1 - \beta \cos \phi)) \right\} \quad (3.2)
 \end{aligned}$$

where $\beta = \sqrt{1 - m_\mu^2/E_\mu^2}$, E_μ is the parent muon energy, $y = E_\nu/E_\mu$, n_μ is the number of useful muons per year obtained from the storage ring and L is the distance to the detector. ϕ is the angle between the beam axis and the direction pointing towards the detector, assumed to be located in the forward direction of the muon beam. As an example, in Fig. 3.2 the neutrino spectra is shown for a parent π^+ of 50 GeV.

Unlike traditional neutrino beams obtained from π and K decays, the fluxes in eq. (3.1), in the forward direction, present a leading quadratic dependence on E_ν .

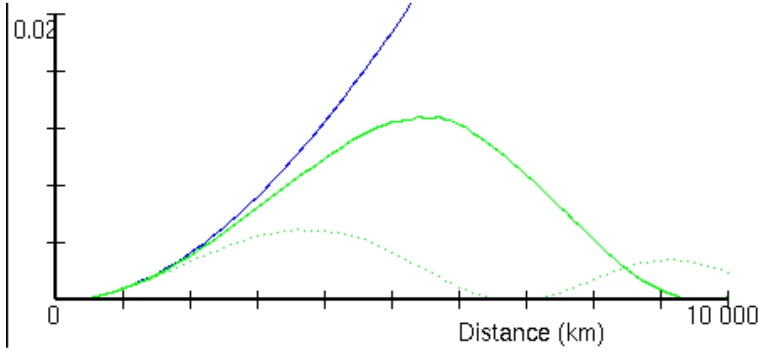


Fig. 3.3: Oscillation probability $\nu_\mu \rightsquigarrow \nu_e$ versus distance, for a neutrino of 30 GeV, without matter effects (blue, higher curve) and with matter effects (green curves, continuous for neutrinos and dotted for antineutrinos).

This comes from the shrinking of the angular opening of the neutrino beam due to the Lorentz boost. Moreover, since the deep-inelastic scattering cross section rises approximately linearly with neutrino energy, and the spectral shape only depends on x , the total number of events observed in a far detector will grow as E_μ^3 . Geometrical solid-angle considerations suggest that, always assuming negligible detector size with respect to the baseline, the flux goes like $1/L^2$. Neglecting matter effects, the oscillation probabilities will depend on L/E_ν , so keeping the same oscillation probability and maximizing the number of events would ideally require very long baselines and large muon energies. The limitation to this, apart from the physical size of the Earth's diameter, comes from the matter effect, that depresses oscillation probabilities for baselines above 4000 km (see Fig. 3.3).

3.5 Wrong Sign Muons

One of the main characteristics of the neutrino factory is that it delivers a well-defined beam free of intrinsic background. For instance, negative muons circulating in the ring will produce ν_μ , that in turn will again produce negative muons in the interaction with the detector. Positive muons are in principle only produced from the oscillation of the $\bar{\nu}_e$ component of the beam. The reversed argument applies for positive muons in the ring. In general, the called right-sign muons are the $\mu^\pm \rightarrow \bar{\nu}_\mu(\nu_\mu) \rightsquigarrow \bar{\nu}_\mu(\nu_\mu) \rightarrow \mu^\pm$, the original muons coming from the beam, and wrong-sign muons the $\mu^\pm \rightarrow \nu_e(\bar{\nu}_e) \rightsquigarrow \nu_\mu(\bar{\nu}_\mu) \rightarrow \mu^\mp$, the muons with a sign originally not present in the beam.

The first exploratory studies of the use of a Neutrino Factory were done in the

context of two-family mixing. In this approximation, the wrong-sign muon signal in the atmospheric range is absent, since the atmospheric oscillation is $\nu_\mu \leftrightarrow \nu_\tau$. The enormous physics reach of such signals in the context of three-family neutrino mixing was only recently realized. The CP-violating phase δ could be at reach. Using muon disappearance measurements, the precision in the knowledge of the atmospheric parameters θ_{23} and $|\Delta m_{23}^2|$ can reach the percent level at a neutrino factory. Furthermore, the sign of Δm_{23}^2 can also be determined at long baselines, through sizeable matter effects.

In practice, other processes can make contributions to the wrong sign muon sample. They are quite rare, but they can become important for low values of θ_{13} . The main backgrounds for a beam produced by μ^- decays are:

- $\bar{\nu}_\mu$ CC events where the right sign muon is lost, and a wrong sign muon is produced by the decay of a π , K or D . The most energetic muons are produced by D decays.
- ν_e CC events where the primary electron is not identified. In this case, D decays are not a major problem since, due to the neutrino helicity, they would produce right sign muons. However, wrong sign muons can come from pion and kaon decay.
- $\bar{\nu}_\mu$ and ν_e NC events where charm production is suppressed with respect to charged currents, and therefore also the main contributions are given by pion and kaon decays.

These backgrounds can be rejected using the facts that muons coming directly from neutrino interactions are higher in energy and more separated from the hadronic jets than those produced in secondary decays. A cut on momentum and on the transverse momentum Q_t of the muon with respect to the jet can reduce the background to wrong sign muons by several orders of magnitude.

3.6 Detection

The measurement of wrong sign muons calls for massive detector weighing $\mathcal{O}(50)$ kton, with the capability of μ identification and the measurement of their charge. There are several technologies that could fulfill that. We will present as an example one of the most promising of such detectors: the Large Magnetized Calorimeter.

3.6.1 A Large Magnetized Calorimeter

The proposed apparatus, shown in Fig. 3.4, is a large cylinder of 10 m radius and 20 m length, made of 6 thick iron rods interspersed with 2 cm thick scintillator

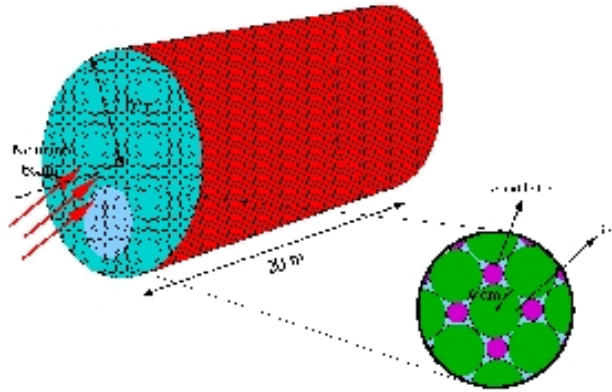


Fig. 3.4: Sketch for the Large Calorimeter for the Neutrino Factory.

rods built of 2 m long segments. The light read-out on both ends allows the determination of the spatial coordinate along the scintillator rod. The detector mass is 40 kton, and a superconducting coil generates a solenoidal magnetic field of 1 T inside the iron. A neutrino traveling through the detector sees a sandwich of iron and scintillator, with the $x - y$ coordinates being measured from the location of the scintillator rods, and the z coordinate from their longitudinal segmentation.

The performance of this detector would be similar to that of MINOS. The main difference lies in the mass, which is an order of magnitude larger, and in the smaller surface-to-volume ratio which together seem to make it superior for the detection of ν_μ and $\bar{\nu}_\mu$ events.

The discrimination of physical backgrounds from the signal is based on the fact that the μ^- produced in a ν_μ CC signal event is harder and more isolated from the hadron shower axis than in background events ($\bar{\nu}_\mu$ CC, ν_e CC, $\bar{\nu}_\mu$ NC and ν_e NC).

3.7 Oscillation Physics at the Neutrino Factory

As was commented before, in principle simply by measuring both $\nu_e \rightsquigarrow \nu_\mu$ and $\bar{\nu}_e \rightsquigarrow \bar{\nu}_\mu$, one can access all of the interesting parameters which describe the neutrino mixing, and so extract all the interesting physics precisely, by simply building a massive detector that can measure the charge and energy of muons.

3.7.1 Oscillation Probabilities in Matter

The exact oscillation probabilities in matter when no mass difference is neglected have been derived analytically by Zaglauer and Schwarzer. However, the physical implications of their formulae are not easily derived. A convenient and precise approximation is obtained by expanding to second order in the following small parameters: θ_{13} , Δ_{13}/Δ_{23} , Δ_{12}/A and $\Delta_{12}L$:

$$\begin{aligned}
 P_{\nu_e \nu_\mu (\bar{\nu}_e \bar{\nu}_\mu)} &= s_{23}^2 \sin^2 2\theta_{13} \left(\frac{\Delta_{13}}{B_{\mp}} \right)^2 \sin^2 \left(\frac{B_{\mp} L}{2} \right) \\
 &+ c_{23}^2 \sin^2 2\theta_{12} \left(\frac{\Delta_{12}}{A} \right)^2 \sin^2 \left(\frac{AL}{2} \right) \\
 &+ J \frac{\Delta_{12}}{A} \frac{\Delta_{13}}{B_{\mp}} \sin \left(\frac{AL}{2} \right) \sin \left(\frac{B_{\mp} L}{2} \right) \cos \left(\pm\delta - \frac{\Delta_{13}L}{2} \right) \quad (3.3)
 \end{aligned}$$

where $\Delta_{ij} = \frac{\Delta m_{ij}^2}{2E\nu}$, $A = \sqrt{2}G_F n_e$ is the matter parameter, $B_{\mp} = |A \mp \Delta_{13}|$ and

$$J \equiv \cos \theta_{13} \sin 2\theta_{13} \sin 2\theta_{23} \sin 2\theta_{12} \quad (3.4)$$

In the limit $A \rightarrow 0$, this expression reduces to the simple formulae in vacuum

$$\begin{aligned}
 P_{\nu_e \nu_\mu (\bar{\nu}_e \bar{\nu}_\mu)} &= s_{23}^2 \sin^2 2\theta_{13} \sin^2 \left(\frac{\Delta_{13}L}{2} \right) \\
 &+ c_{23}^2 \sin^2 2\theta_{12} \sin^2 \left(\frac{\Delta_{12}L}{2} \right) \\
 &+ J \cos \left(\pm\delta - \frac{\Delta_{13}L}{2} \right) \frac{\Delta_{12}L}{2} \sin \left(\frac{\Delta_{13}L}{2} \right) \quad (3.5)
 \end{aligned}$$

Matter effects induce an asymmetry between neutrinos and antineutrinos oscillation probabilities even for vanishing δ . For this reason, a CP-odd asymmetry would not be the most transparent observable.

In the standard decomposition of the PMNS matrix, it is the second rotation matrix the one that contains the angle θ_{13} , which acts as a link between the atmospheric and solar realms. It also contains the CP-violation phase δ . We know from experimental data that θ_{13} is small, and we know from solar and atmospheric experiment that there exists a strong mass hierarchy in the neutrino sector ($\Delta m_{23}^2 \gg \Delta m_{12}^2$). The consequence is that solar and atmospheric oscillations approximately decouple in two 2-by-2 mixing phenomena which results in the second matrix in the parameterization of the PMNS matrix becoming the identity matrix.

Most experiments until now have been sensitive either to the atmospheric or the solar parameters. What makes the neutrino factory unique is precisely its ability to measure or set very stringent limits on these both parameters, θ_{13} and δ .

3.7.2 Precision Measurement of Known Oscillations

The parameters governing the leading atmospheric oscillation $\nu_\mu \rightsquigarrow \nu_\tau$, θ_{23} and Δm_{23}^2 , can be measured to an unprecedented precision. These parameters are mainly determined from the disappearance of muon neutrinos in the beam, observed using right sign muon events. The maximum of the oscillation probability will produce a dip in the visible spectrum. The energy position of this dip will be correlated to the value of Δm_{23}^2 , and the depth to θ_{23} . It is therefore favorable to choose an energy and baseline such that the maximum of the oscillation probability lies comfortably inside the detectable spectrum.

The precision on the measurement of the oscillation parameters has been addressed by several groups, and is normally performed by a fit on the energy spectra of the event classes. The expected precisions are of 1% for Δm_{23}^2 and of 10% for $\sin^2 \theta_{23}$.

3.7.3 Sensitivity to θ_{13}

So far, the most accurate information on θ_{13} is the CHOOZ limit $\sin^2 2\theta_{13} < 0.11$. In a favorable case, a non-zero value of this parameter could be discovered before the Neutrino Factory by experiments running in first-generation neutrino beams, such as ICARUS and MINOS. Much larger sensitivity will however be achieved by Superbeams, for instance the JHF-Super-Kamiokande project. But experiments performed with conventional beams from pion decays will always be limited by the presence of a ν_e component in the beam itself, representing an irreducible background to the search for $\nu_\mu \rightarrow \nu_e$ oscillations.

On the other hand, the Neutrino Factory would have a significantly improved sensitivity to θ_{13} thanks to the wrong sign muon signal, that measures the oscillation $\nu_e \rightsquigarrow \nu_\mu$, where the oscillated muon neutrinos are easily separated from the beam component of opposite sign by measuring the charge of the produced muon.

Applying strong cuts on muon momentum and isolation, the background from the decays of charmed particles, kaons and pions, can be reduced by as much as a factor 10^6 , keeping an efficiency of about 40%.

The parameter θ_{13} is extracted from a fit to the energy distribution of the wrong sign muons. Moreover, from the formula of the oscillation probability we see that the value of θ_{13} has a limited influence on the spectral shape, and even factorizes

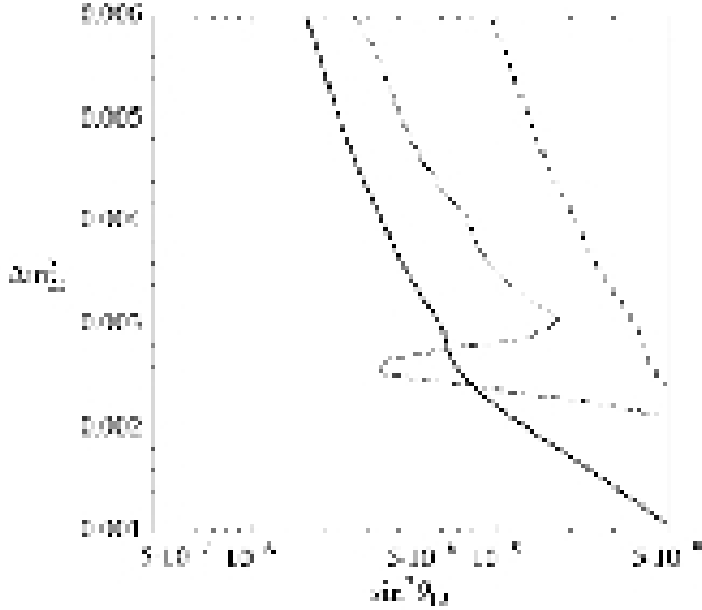


Fig. 3.5: Sensitivity to $\sin^2 \theta_{13}$ for a magnetized iron detector, with realistic backgrounds. The three lines correspond to baselines of 730 (dashed), 3500 (solid) and 7300 km (dotted).

out from the energy dependence in the approximation $\Delta m_{12}^2 = 0$, so most of the information actually comes from just counting wrong sign muon events.

The background level is the ultimate limiting factor for this measurement, and the sensitivity would be of the order of $\sin^2 \theta_{13} \sim 5 \times 10^{-5}$ (see Fig. 3.5).

3.7.4 Sensitivity to CP violation

Detecting the presence of a complex phase in the leptonic mixing matrix is one of the most ambitious goals of neutrino physics, and would justify the effort of building a neutrino factory.

In eq. (3.3) it is seen that the term with δ is only suppressed in the parameters Δm_{12}^2 and θ_{13} . Since the CP-even parts of the probabilities are always larger than the CP-odd parts, they dominate the number of events and thus the error on the measured asymmetry.

Due to the small energy dependence induced by CP violation, the use of spectral information to have a simultaneous measurement of δ and θ_{13} is not very ef-

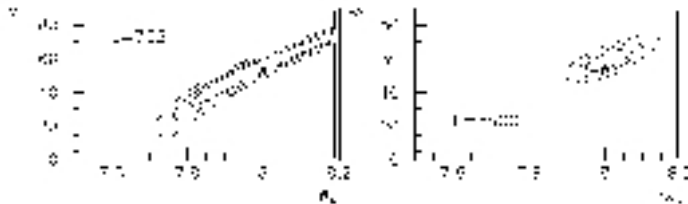


Fig. 3.6: Contour plots resulting from a χ^2 fit of θ_{13} and δ , at 1, 2 and 3 σ . The parameters used to generate the data are depicted by a star, and the baseline which is used for the fit indicated in each plot.

fective, and only helps under some conditions. The simultaneous fits in θ_{13} and δ reveal for most of the cases a strong correlation between the two parameters (see Fig. 3.6).

3.8 Propaganda

The neutrino beams obtained from muon storage rings will be excellent for precision neutrino physics. The appearance of wrong sign muons is a powerful neutrino oscillation signal, which allows to improve considerably our knowledge of the leptonic flavor sector.

The Neutrino Factory offers unequalled reach for all the basic open questions: the magnitude of θ_{13} , CP violation and matter effects. Several important questions about the design of a Neutrino Factory remain to be answered, notably muon cooling. Even without cooling, there is an exciting program of experiments with slow or stopped muons that complements the neutrino oscillation program described here. If muon cooling can be perfected beyond the requirements of the neutrino factory, a muon collider may become feasible, offering exciting options in Higgs physics and/or high-energy lepton collisions.

4. NEAR FUTURE: SUPERBEAMS

The notion of “super beams” was introduced by Richter [7], who suggested that a conventional neutrino beam of very high intensity could be competitive with the pure two-flavor neutrino beams produced by the Neutrino Factory. Thanks to the fact that the solution to the solar anomaly has been confirmed to be in the LMA region, a Superbeam could largely improve our knowledge of Δm_{23}^2 , θ_{23} and θ_{13} , as well as provide some sensitivity to the CP violating phase δ . On the other hand, the ultimate sensibility to these parameters, in particular to δ , will still require the pure and intense beams of a neutrino factory.

4.1 Rationale

The signal to noise ratio in an experiment looking for the appearance of a type of neutrino not initially present in the beam, in a two-neutrino model, is:

$$\frac{P(\nu_1 \rightsquigarrow \nu_2)}{P(\nu_1 \rightsquigarrow \nu_1)} = \frac{A^2 \sin^2(\Delta m^2 L/4E)}{1 - A^2 \sin^2(\Delta m^2 L/4E)} \quad (4.1)$$

where A is the mixing amplitude, Δm^2 is the difference of the squares of the masses, L is the distance from the source to the detector, and E is the beam energy. The optimum signal to noise ratio comes when the sine term is equal to one: $\Delta m^2 L/4E = (2n + 1)\pi/2$. However, all of the muon storage ring designs have high energy, making this factor small with the known mass differences. On the other hand, a conventional low-energy beam can be tuned to make it maximum.

Neutrino cross sections increase approximatively linear with the energy, and the flux of neutrinos increases with the square of the energy of the parent particle. This gives an overall factor E^3 that makes going to high energy very appealing. However, in an experiment looking for the appearance of a neutrino species different from the primary species (as is the golden channel in a Neutrino Factory), the probability is proportional to E^{-2} , so there is only an overall E factor in the improvement of Neutrino Factories versus conventional beams.

These considerations and the big cost of a Neutrino Factory spurred the interest in a thorough study of Superbeams as alternatives to the Neutrino Factory.

4.2 Generation of Superbeams

A conventional neutrino beam is produced by hitting a nuclear target with an intense hadron beam, then sign-selecting and letting decay the resulting hadrons through a beam decay tunnel. At the end of the tunnel there is an absorber, where the copiously produced muons, a byproduct of pion and kaon decay, are ranged out before most of them can decay.

The resulting neutrino beam is mostly made of ν_μ (assuming that π^+ were selected). Nevertheless, kaon and muon decays result in small but sizeable contamination of ν_e and $\bar{\nu}_e$. Opposite sign pion feed-through yields also some contamination of $\bar{\nu}_\mu$. Fig. 4.1 shows a typical composition for these kind of neutrino beams.

The contamination of other neutrino species is a handicap for the neutrino oscillation appearance experiments, in which one searches for a flavor not originally in the beam. Indeed this is the key advantage of neutrino factory beams, over conventional beams.

A Superbeam is just a conventional beam of enormous intensity. Thus, for π^+ selected in the horn, its basic composition is ν_μ with small admixtures of ν_e , $\bar{\nu}_e$ and $\bar{\nu}_\mu$. To gain some appreciation of the relative sensitivity of a conventional neutrino beam and a neutrino factory beam, it is useful to estimate the sensitivity to a $\nu_\mu \rightsquigarrow \nu_e$ oscillation search in the appearance mode, assuming a perfect detector. In a neutrino factory the sensitivity goes as

$$P_{\nu_\mu\nu_e} \propto \frac{1}{N_\mu} \quad (4.2)$$

where N_μ is the number of ν_μ visible interactions registered by the apparatus. This is because there is no ν_e contamination.

On the other hand, in the case of a conventional beam,

$$P_{\nu_\mu\nu_e} \propto \frac{\sqrt{N_e}}{N_\mu} \quad (4.3)$$

so that if the ν_e contamination is a fraction f of the primary ν_μ beam (assuming for simplicity identical ν_e and ν_μ cross sections) we have:

$$P_{\nu_\mu\nu_e} \propto \frac{\sqrt{f}}{\sqrt{N_\mu}} \quad (4.4)$$

Although \sqrt{f} is a small quantity, the key difference between conventional and muon-induced beams is clear comparing both equations. In the first case the sensitivity improves linearly while in the second improves only with the square root of the total collected statistics.

Another issue concerns systematics in beam composition. While the neutrino spectra from muon decay can be computed to a great precision, the convoluted spectra in a conventional beam are affected by a number of uncertainties, the most important of which is the initial π/K ratio in the hadron beam, which affects the composition of the beam. Typically, these and other uncertainties translate into a systematic error at the level of few per cent in the conventional neutrino fluxes, to be compared with a few per mil in the case of a neutrino factory.

Other important aspects to be considered when designing a conventional beam are whether one prefers a wide or narrow band beam and the energy regime. Beam energies range typically from few hundred MeV to few hundred GeV, depending on the colliding hadron beam and beam optics. High energy yields more interactions, but sufficiently low energy yields a better control over backgrounds and less beam uncertainties.

4.3 The SPL neutrino beam

The planned Super Proton Linac is a proton beam of 4 MW power which will be used as a first stage of the Neutrino Factory complex. Pions are produced by the interactions of the 2.2 GeV proton beam with a liquid mercury target and focused (or defocused, depending on the sign) with a magnetic horn. Next they transverse a cylindrical decay tunnel of 1 m radius and 20 m length.

The spectra is shown in Fig. 4.1. The average neutrino energy is around 250 MeV, and the ν_e contamination of the beam is at the level of few per mil. Due to the low energy of protons, kaon production is strongly suppressed, resulting in both less ν_e contamination and better controlled beam systematics.

4.4 Detection

Fig. 4.2 shows the oscillation probability $P_{\nu_\mu\nu_e}$ as a function of the distance. The first maximum of the oscillation is at 100 km. Detection of low energy neutrinos at $\mathcal{O}(100km)$ from the source requires a massive target with high efficiency. Moreover, a search for ν_e appearance demands excellent rejection of physics backgrounds, namely μ misidentification and neutral current π^0 production, which should be controlled to a lower level than the irreducible beam-induced background.

Two technologies that have demonstrated excellent performance in the low energy regime while begin able to provide massive targets are water Cerenkov detectors and diluted liquid scintillator detectors.

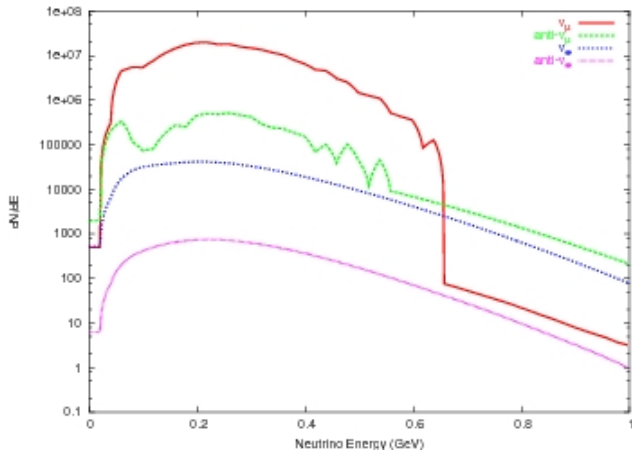


Fig. 4.1: Fluxes of the CERN SPL. Notice that the beam is mostly made of ν_μ but there are contaminations of all other neutrino species, except ν_τ .

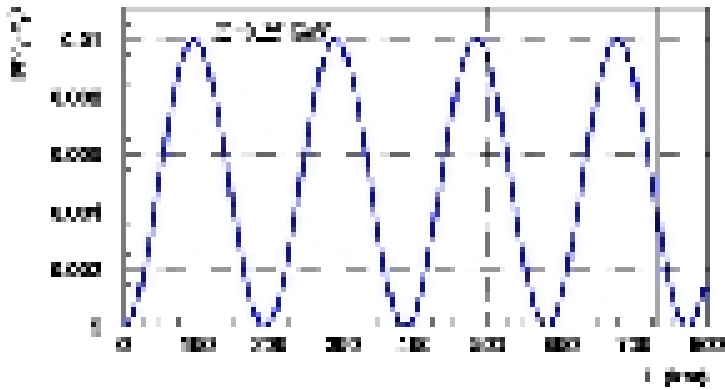


Fig. 4.2: Oscillation probability P_{ν_μ, ν_e} for a neutrino of 250 MeV. The first maximum lies around 100 km.

In spite of the fact that liquid scintillator detectors provide, a priori, more handles to reject backgrounds than their water Cerenkov counterparts, the only truly massive detectors built so far are of the latest type.

4.4.1 Water Cerenkov Detectors

An example of this kind of detectors is Super-Kamiokande, with its 40 kton of fiducial mass. The response of the detector to the neutrino beams was studied with the NUANCE neutrino physics generator and reconstruction algorithms developed for the Super-Kamiokande atmospheric neutrino analysis.

In the absence of neutrino oscillations, the dominant reaction induced by the beam is ν_μ quasielastic scattering, leading to a single observed muon ring. Recoiling protons are well below Cerenkov threshold at the energies of the SPL-generated neutrinos, and hence produce no rings. To unambiguously identify a potentially small ν_e appearance signal, it is essential to avoid confusion of muons with electrons. Thanks to the low energy of the SPL and its neutrino beam, the Cerenkov threshold itself helps separate muons and electrons, since a muon produced near the peak of the spectrum ($\sim 300\text{MeV}$) cannot be confused with an electron of comparable momentum; instead it will appear to be a much lower energy ($\sim 100\text{MeV}$) electron.

Particle identification exploits the difference in the Cerenkov patterns produced by the showering (“e-like”) and non-showering (“ μ -like”) particles. Besides, for the energies of interest in this beam, the difference in Cerenkov opening angle between an electron and a muon can also be exploited. Furthermore, muons which stop and decay produce a detectable delayed electron signature which can be used as an additional handle for background rejection.

Production of π^0 through neutral current resonance-mediated and coherent processes is another major source of background, which is, however, suppressed by the low energy of the beam and the relatively small boost of the resulting π^0 . This results in events where the two rings are easily found by a standard π^0 search algorithm.

4.5 Sensitivity

To illustrate the sensitivity of a Superbeam we will use a 40 kton water or liquid oil detector located at 130 km from the source. Actually, the last designs for Superbeams that are under consideration include much bigger detectors, UNO-style, of about 400 kton.

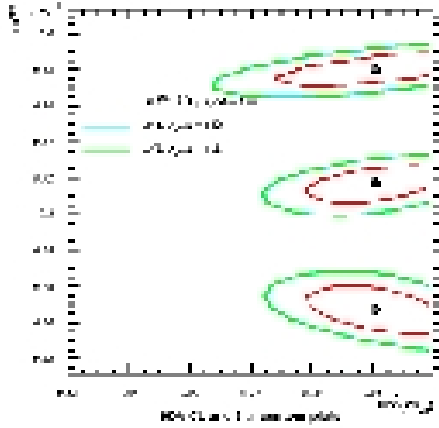


Fig. 4.3: Fits in the $\Delta m_{23}^2, \sin^2 2\theta_{23}$ plane after 5 years of run, for a systematic uncertainty of 2%. The crosses sign the initial points in coordinates.

4.5.1 Sensitivity to the Atmospheric Parameters

A 40 kton detector has excellent opportunities of precision measurements of $\sin^2 \theta_{23}$ and Δm_{23}^2 with a ν_μ disappearance experiment. Given the mean beam energy of the ν_μ beam, $(1.27L/E)^{-1} = 1.6 \times 10^{-3} eV^2$, and $P_{\nu_\mu \nu_\mu}$ is just at its minimum.

To illustrate the precision in measuring Δm_{23}^2 and θ_{23} in case of positive signal, Fig. 4.3 shows the result of 5 years exposure in case the oscillation occurs with $\sin^2 2\theta_{23} = 0.98$ and $\Delta m_{23}^2 = 3.8, 3.2$ or $2.5 eV^2$. To make the reconstruction it is not possible to bin much in energy, due to the smearing caused by the Fermi motion.

4.5.2 Sensitivity to CP violation

Unfortunately for a water Cerenkov detector, the $\bar{\nu} + {}^{16}O$ cross-section is approximately six times less than that for $\nu + {}^{16}O$ at these energies, diminishing the experiment's sensitivity to CP violation.

Because of the big correlations between θ_{13} and δ , a simultaneous fit of both parameters is convenient. Fig. 4.4 shows the confidence level contours for a simulation fit of θ_{13} and δ , corresponding to the three values of $\theta_{13} = 5^\circ, 8^\circ, 10^\circ$ and a maximal CP violation phase of $\delta = \pm 90^\circ$. Since the sensitivity is dominated by the low antineutrino statistics, this is done for a 10 year run with focused π^- and a 2 year run with π^+ .

From the same figure it is possible to see that the sensitivity to δ does not

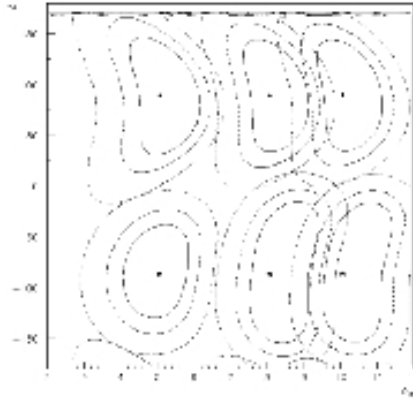


Fig. 4.4: 1,2 and 3 σ confidence level intervals resulting from a simultaneous fit to the θ_{13} and δ parameters. The generated values are $\theta_{13} = 5^\circ, 8^\circ, 10^\circ$ and $\delta = \pm 90^\circ$. The detector mass is 40 kton.

worsen very much when θ_{13} becomes (moderately) smaller. Also, at 90% confidence level, a maximally violating CP phase $\delta = \pm 90^\circ$ would be just distinguishable from a non CP violating phase $\delta = 0^\circ$. So this experiment would offer a chance to observe CP violation only on a very lucky scenario.

Fig. 4.5 shows the result of the same fit for a very large water detector, such as the proposed UNO water Cerenkov, with a fiducial mass of 400 kton. Clearly, the prospects to observe CP violation are much improved.

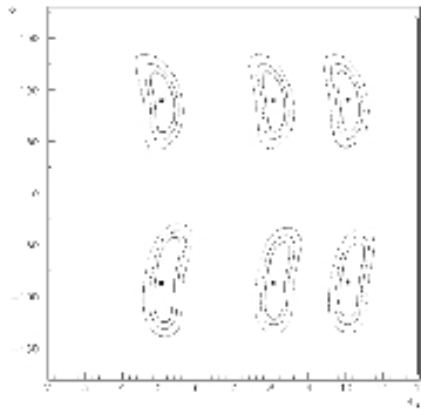


Fig. 4.5: 1,2 and 3 σ confidence level intervals resulting from a simultaneous fit to the θ_{13} and δ parameters. The generated values are $\theta_{13} = 5^\circ, 8^\circ, 10^\circ$ and $\delta = \pm 90^\circ$. The detector mass is 400 kton.

5. CORRELATIONS, DEGENERACIES, COMBINATIONS

5.1 Correlations

The oscillation probability formulae couple the set of parameters θ_{12} , θ_{23} , θ_{13} , δ , Δm_{12}^2 , and Δm_{23}^2 . In general, when one experiment tries to measure several parameters simultaneously, the uncertainty in each measured parameter will depend on the real (but only measured up to a certain degree) value of all the others. The parameters are correlated in the sense that an experiment is dominantly sensitive to a certain parameter combination. Weaker information on other parameter combinations allows typically to disentangle the parameters, but some correlations survive.

As an example, the measurement of a sum $a + b$ does not determine the individual values of a and b . Some more small information on other combinations of a and b produce potato-shaped regions aligned along $a + b = \text{const}$.

The value of a parameter and its uncertainty is merely the projection of the allowed region on the axis of that parameter, which will be bigger in general than the allowed region for the rest of the parameters equal to their central values (see Fig. 5.1).

5.2 Degeneracies

Degeneracies occur when two or more separated sets fit the same data (see for example Fig. 5.2). Dealing with degeneracies, one might, for example, either quote separate uncertainties for completely separated parameter sets, or take the whole range covered by the degeneracies as the measurement uncertainty.

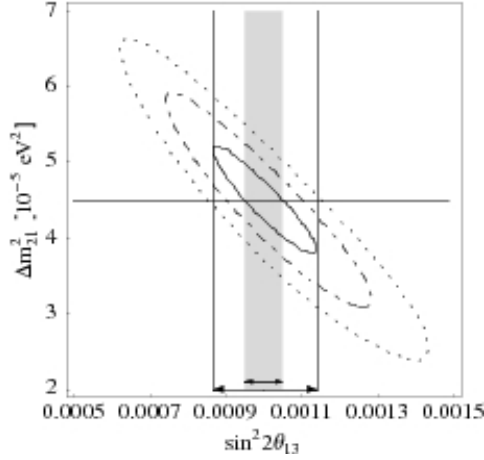


Fig. 5.1: 1σ , 2σ and 3σ contours of the χ^2 -function for a fit in $(\Delta m_{23}^2, \sin^2 2\theta_{13})$. The vertical lines indicate the ‘extra’ overall uncertainty in $\sin^2 2\theta_{13}$ coming from the correlation with Δm_{12}^2 [19].

5.3 Status at the Neutrino Factory

The best way to measure δ and θ_{13} is through the sub-leading transitions $\nu_e \leftrightarrow \nu_\mu$ and $\bar{\nu}_e \leftrightarrow \bar{\nu}_\mu$. They can be measured, for instance, at a neutrino factory by searching for wrong-sign muons while running in both polarities of the beam, i.e. μ^+ and μ^- respectively.

The exact oscillation probabilities in matter when no mass difference is neglected can be approximated expanding the exact formulas to second order in the small parameters θ_{13} , Δ_{12}/Δ_{23} , Δ_{12}/A and $\Delta_{12}L$ (where $\Delta_{ij} \equiv \frac{\Delta m_{ij}^2}{2E}$):

$$\begin{aligned}
 P_{\nu_e \nu_\mu (\bar{\nu}_e \bar{\nu}_\mu)} &= s_{23}^2 \sin^2 2\theta_{13} \left(\frac{\Delta_{13}}{B_\mp} \right)^2 \sin^2 \left(\frac{B_\mp L}{2} \right) \\
 &+ c_{23}^2 \sin^2 2\theta_{12} \left(\frac{\Delta_{12}}{A} \right)^2 \sin^2 \left(\frac{AL}{2} \right) \\
 &+ J \frac{\Delta_{12}}{A} \frac{\Delta_{13}}{B_\mp} \sin \left(\frac{AL}{2} \right) \sin \left(\frac{B_\mp L}{2} \right) \cos \left(\pm\delta - \frac{\Delta_{13}L}{2} \right)
 \end{aligned} \tag{5.1}$$

where L is the baseline, $B_\mp \equiv |A \mp \Delta_{13}|$ and the matter parameter, A , is given in terms of the average electron number density, $n_e(L)$, as $A \equiv \sqrt{2}G_F n_e(L)$. J is defined as

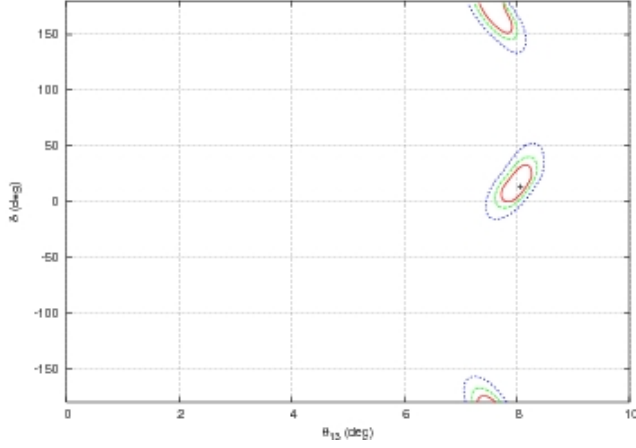


Fig. 5.2: 1σ , 2σ and 3σ contours of the χ^2 -function for a fit in (θ_{13}, δ) . For the central values $\theta_{13} = 8^\circ$ and $\delta = 15^\circ$, a second solution appears, affecting our knowledge of δ .

$$J \equiv \cos \theta_{13} \sin 2\theta_{13} \sin 2\theta_{23} \sin 2\theta_{12} \quad (5.2)$$

In the limit $A \rightarrow 0$, this expression reduces to the simple formulae in vacuum

$$\begin{aligned} P_{\nu_e \nu_\mu}(\bar{\nu}_e \bar{\nu}_\mu) &= s_{23}^2 \sin^2 2\theta_{13} \sin^2 \left(\frac{\Delta_{13}L}{2} \right) \\ &+ c_{23}^2 \sin^2 2\theta_{12} \sin^2 \left(\frac{\Delta_{12}L}{2} \right) \\ &+ J \cos \left(\pm\delta - \frac{\Delta_{13}L}{2} \right) \frac{\Delta_{12}L}{2} \sin \left(\frac{\Delta_{13}L}{2} \right) \end{aligned} \quad (5.3)$$

The three terms in 5.1 will be called the atmospheric, $P_{\nu(\bar{\nu})}^{atm}$, solar, P^{sol} , and interference term, $P_{\nu(\bar{\nu})}^{inter}$.

An immediate result is

$$|P_{\nu(\bar{\nu})}^{inter}| \leq P_{\nu(\bar{\nu})}^{atm} + P^{sol} \quad (5.4)$$

implying two very different regimes. When θ_{13} is relatively large or Δm_{12}^2 small, the probability is dominated by the atmospheric term, since $P_{\nu(\bar{\nu})}^{atm} \gg P^{sol}$. This situation is referred as the atmospheric regime. Conversely, when θ_{13} is very small or Δm_{12}^2 large, the solar term dominates $P^{sol} \gg P_{\nu(\bar{\nu})}^{atm}$. This is the solar

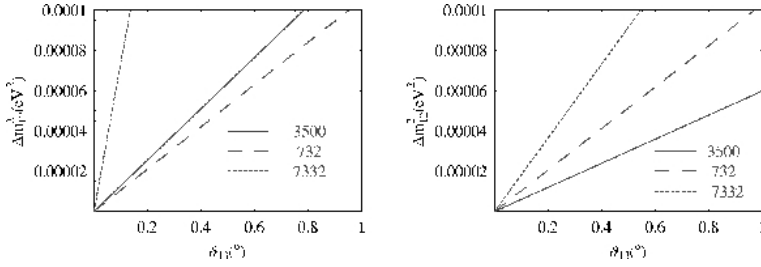


Fig. 5.3: Contours $P_{\nu}^{atm} = P^{sol}$ (left) and $P_{\bar{\nu}}^{atm} = P^{sol}$ (right) on the plane (θ_{13}, δ) , for three reference baselines.

regime. Fig. 5.3 illustrates the separation between the two regimes on the plane $(\Delta m_{12}^2, \theta_{13})$ for neutrinos and antineutrinos, as derived from eq. (5.1). The area to the right (left) of the curves corresponds to the atmospheric (solar) regime.

5.3.1 Correlation Between δ and θ_{13}

The oscillation probabilities of eq. (5.1), from whose measurement δ could be extracted, depend as well on θ_{23} , Δm_{23}^2 , θ_{12} , Δm_{12}^2 , A and θ_{13} . Uncertainties in the latter quantities can then hide the effect of CP violation. Although the first five of these parameters are expected to be well known at the time of the neutrino factory with a good accuracy, θ_{13} might well remain unknown. It is essential then to understand whether the correlation between θ_{13} and δ can be resolved in such a way that CP violation is measurable.

For a single beam polarity and a fixed neutrino energy and baseline, the expansion of eq. (5.1) to second order in θ_{13} leads to

$$P_{\nu_e \nu_\mu}(\bar{\nu}_e \bar{\nu}_\mu) = X_{\pm} \theta_{13}^2 + Y_{\pm} \theta_{13} \cos\left(\pm\delta - \frac{\Delta_{13} L}{2}\right) + P^{sol} \quad (5.5)$$

with obvious assignments for the coefficients X and Y , which are independent of θ_{13} and δ . Note that the solar term P^{sol} is the same for neutrinos and antineutrinos.

As eq. (5.5) is a function of 2 parameters, θ_{13} and δ , there is a continuum of pair of values (θ_{13}, δ) that give the same probability than the real values $(\bar{\theta}_{13}, \bar{\delta})$.

This requirement can be solved simply for θ_{13} as a function of δ :

$$\theta_{13} = -\frac{Y_+}{2X_+} \cos\left(\delta - \frac{\Delta_{13} L}{2}\right)$$

$$\pm \sqrt{\left(\frac{Y_+}{2X_+} \cos\left(\delta - \frac{\Delta_{13}L}{2}\right)\right)^2 + \frac{1}{X_+}(P_{\nu_e\nu_\mu}(\bar{\theta}_{13}, \bar{\delta}) - P^{sol})} \quad (5.6)$$

Eq. (5.6) is a curve of equal probability on the plane (θ_{13}, δ) , which for most of the parameter space spans the whole range of δ . It follows that, at any baseline, it is not possible to determine δ with the measurement of wrong-sign muons at a fixed neutrino energy with a single beam polarity.

The analogous case for antineutrinos is a different equal probability curve, with the substitutions in (5.6): $\delta \rightarrow \bar{\delta}$, $X_+(Y_+) \rightarrow X_-(Y_-)$.

When finite uncertainties are taken into account, the shapes of the χ^2 -allowed regions are two broad bands with close paths. The intersection of these two regions will result in one region where θ_{13} and δ are correlated.

5.3.2 Intrinsic Degeneracies

If both the neutrino and antineutrino oscillation probabilities have been measured, at fixed (anti)neutrino energy and baseline, the two equal-probability curves may intersect at values of (θ_{13}, δ) different from $(\bar{\theta}_{13}, \bar{\delta})$. This condition implies equation (5.6) to the corresponding one for antineutrinos and solving for δ , for small $\theta_{13} > 0$. The resulting equation is rather complicated, but simplifies considerably in the atmospheric and extreme solar regimes.

Atmospheric Regime

In this regime it is safe to keep terms only up to first order in $Y_+/X_+(Y_-/X_-)$ in eq. (5.6). As a result only the solution of eq. (5.6) with + sign in front of the square root is acceptable since $\theta_{13} > 0$. Eq. (5.6) simplifies to

$$\theta_{13} = \bar{\theta}_{13} - \frac{Y_+}{2X_+} \left[\cos\left(\delta - \frac{\Delta_{13}L}{2}\right) - \cos\left(\bar{\delta} - \frac{\Delta_{13}L}{2}\right) \right] \quad (5.7)$$

The equation for δ is then obtained from equating (5.7) for neutrinos to that for antineutrinos. The problem amounts to finding the roots of a function of δ which is continuous and periodic. Since it must have at least one root at $\delta = \bar{\delta}$, by periodicity there must be at least a second root in the range $-180^\circ < \delta < 180^\circ$

The second solution for δ in this approximation is:

$$\begin{aligned} \sin \delta - \sin \bar{\delta} &= -2 \frac{\sin \bar{\delta} - z \cos \bar{\delta}}{1 + z^2} \\ \cos \delta - \cos \bar{\delta} &= 2z \frac{\sin \bar{\delta} - z \cos \bar{\delta}}{1 + z^2} \end{aligned} \quad (5.8)$$

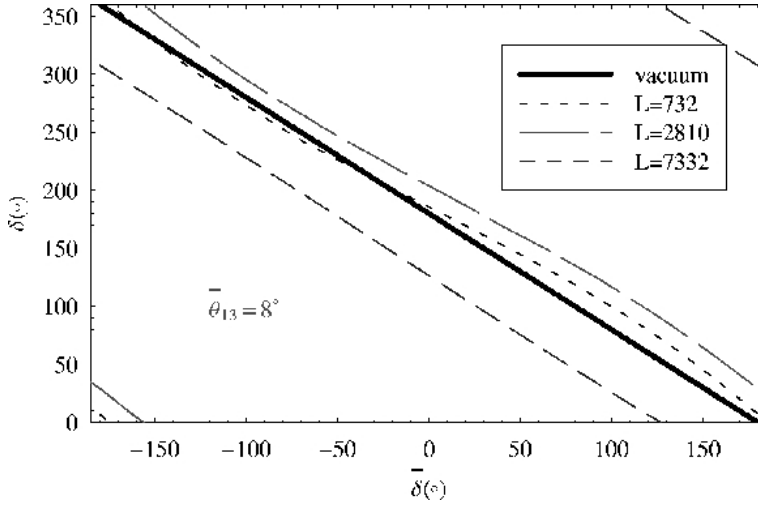


Fig. 5.4: Degenerate value of δ as a function of true value $\bar{\delta}$, for $\bar{\theta}_{13} = 8^\circ$ and three different baselines. The vacuum result $\delta = \pi - \bar{\delta}$ is also shown.

where $z \equiv \frac{C_+}{C_-} \tan \frac{\Delta_{13}L}{2}$ and $C_\pm \equiv \frac{1}{2} \left(\frac{Y_+}{X_+} \pm \frac{Y_-}{X_-} \right)$. The corresponding value of θ_{13} is:

$$\theta_{13} = \bar{\theta}_{13} - \frac{1}{2} \frac{\sin \bar{\delta} - z \cos \bar{\delta}}{1 + z^2} \frac{C_+^2 - C_-^2}{C_-} \sin \frac{\Delta_{13}L}{2} \quad (5.9)$$

Only for the value of $\bar{\delta}$ satisfying

$$\tan \bar{\delta} = z \quad (5.10)$$

do the two solutions degenerate into one. Except for this particular point, there are two degenerate solutions with the penalty that, in an unfortunate value of $\bar{\delta}$, one solution may correspond to CP-conservation and its image not.

In vacuum this is not the case. Eq. (5.8) in the vacuum limit: $C_- \rightarrow 0$ or $z \rightarrow \infty$, gives $\delta = \pi - \bar{\delta}$ so that only for $\bar{\delta} = \pm\pi/2$ there is no degeneracy. Then the two solutions either break or conserve CP.

In Fig. 5.4 is shown the value of δ as a function of $\bar{\delta}$ for $\bar{\theta}_{13} = 8^\circ$ for three reference baselines together with the vacuum result. The difference between δ and $\bar{\delta}$ is maximal close to $\bar{\delta} = 0^\circ, 180^\circ$.

It is interesting to consider the different impact of these degenerate solutions at different baselines. At short baselines, the oscillation probabilities for neutrinos and antineutrinos are approximately the same for two reasons: 1) the relative size

of the $\sin \delta$ versus $\cos \delta$ term in eq. (5.1) is $\tan(\Delta_{13}L/2) \ll 1$, 2) matter effects are irrelevant with the solutions approaching the vacuum case. Indeed, the expansion of Eq. (5.7) for $\Delta_{13}L/2 \ll 1$ simplifies to

$$\theta_{13} \simeq \bar{\theta}_{13} - \frac{Y_+}{2X_+}(\cos \delta - \cos \bar{\delta}) \quad (5.11)$$

The same equation holds for antineutrinos, since $X_+(Y_+) = X_-(Y_-)$ in this approximation. The two equations have collapsed into one, and consequently one expects to find a continuum curve of solutions (θ_{13}, δ) of the approximate form given by eq. (5.11). As the baseline increases the probabilities for neutrino and antineutrino oscillations start to differ, not only due to the term in $\sin \delta$, but also because of the matter effects. A shift in δ cannot in general be then compensated in the neutrino and antineutrino probabilities by a common shift of θ_{13} , and only the two-fold degeneracy discussed above survives.

Solar Regime

In this regime the second term in eq. (5.1) dominates, although the first term cannot be neglected in the analysis of degenerate solutions even for very small values of $\bar{\theta}_{13}$. The reason is that there exist, at fixed neutrino energy and baseline, a pair of values (θ_{13}, δ) at which the first and third terms in eq. (5.1) exactly compensate both for neutrinos and antineutrinos, in such a way that they are indistinguishable from the situation with $\bar{\theta}_{13} = 0$ and any $\bar{\delta}$. It is easy to find these values by setting $\bar{\theta}_{13} = 0$ in eq. (5.6) and in the equivalent equation for antineutrinos. δ is the solution of:

$$\tan \delta = -\frac{1}{z} \quad (5.12)$$

and the corresponding θ_{13} is:

$$\theta_{13} = -\frac{Y_+}{X_+} \cos \left(\delta - \frac{\Delta_{13}L}{2} \right) \quad (5.13)$$

Taking as an example $\Delta m_{23}^2 = 3 \times 10^{-3} eV^2$, $L = 2810$ km and $E_\nu = 0.3E_\mu$, $E_\mu = 50$ GeV, this point is:

$$\theta_{13} \sim 1.5^\circ, \quad \delta \sim -165^\circ \quad (5.14)$$

Alike to the pattern in the atmospheric regime, this degeneracy occurs only at fixed neutrino energy and baseline.

In summary, even with the information from both beam polarities, there are in general two equally probable solutions, at fixed neutrinos energy and baseline, for the parameters θ_{13} and δ .

5.3.3 Simultaneous Determination of δ and θ_{13}

The observables used to determine δ and θ_{13} simultaneously are the number of wrong-sign muons in five bins of energy for both beam polarities:

$$N_{i,\pm} \quad (5.15)$$

where i labels the energy bin, and \pm the sign of the decaying muons. These numbers are given by:

$$N_{i,\pm} = \int_{E_i}^{E_i+\Delta E} \Phi_{\nu(\bar{\nu})}(E_\nu, L) \sigma_{\nu(\bar{\nu})}(E_\nu) P_{\nu(\bar{\nu})}(E_\nu, L, \theta_{13}, \delta, \alpha) \quad (5.16)$$

where α is the set of remaining oscillation parameters: $\theta_{23}, \theta_{12}, \Delta m_{23}^2, \Delta m_{12}^2$ and the matter parameter A , which are taken as known. $\Phi_{\nu(\bar{\nu})}$ denote the neutrino fluxes and $\sigma_{\nu(\bar{\nu})}$ the deep inelastic scattering cross sections.

With these observables, the χ^2 fits of the parameters δ and θ_{13} are obtained from:

$$\chi^2 = \sum_{i,j} \sum_{p,p'} (n_{i,p} - N_{i,p}) C_{i,p;j,p'}^{-1} (n_{j,p'} - N_{j,p'}) \quad (5.17)$$

where C is the $2N_{bin} \times 2N_{bin}$ covariance matrix. $n_{i,j}$ are the simulated ‘‘data’’ obtained from a Gaussian or Poisson smearing including backgrounds and efficiencies. For a correct analysis that takes the correlations into account, the form of the matrix C is:

$$C_{i,p;j,p'} \equiv \delta_{ij} \delta_{pp'} (\delta n_{i,p})^2 + \sum_{\alpha} \frac{\partial N_{i,p}}{\partial \alpha} \frac{\partial N_{j,p'}}{\partial \alpha} \sigma^2(\alpha) \quad (5.18)$$

where $\sigma(\alpha)$ is the 1σ uncertainty on the parameter α .

Atmospheric Regime

In Figs. 5.5 we can see the results of the fits including efficiencies and backgrounds for $L = 2810$ km for central values of $\bar{\delta} = -90^\circ, 0^\circ, 90^\circ, 180^\circ$ and for $\theta_{13} = 2^\circ$ (left) and $\bar{\theta}_{13} = 8^\circ$ (right). The energy dependence of the signals is not significant enough (with this setup) to resolve the expected two-fold degeneracy. The second

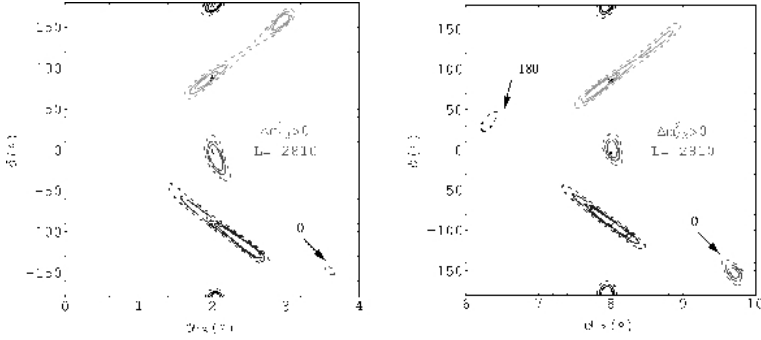


Fig. 5.5: Simultaneous fits of δ and θ_{13} at $L = 2810$ km for different central values (indicated by the stars) of $\bar{\delta} = -90^\circ, 0^\circ, 90^\circ, 180^\circ$ and $\bar{\theta}_{13} = 2^\circ$ (left), 8° (right). The value of $\bar{\delta}$ for the degenerate solutions is also indicated.

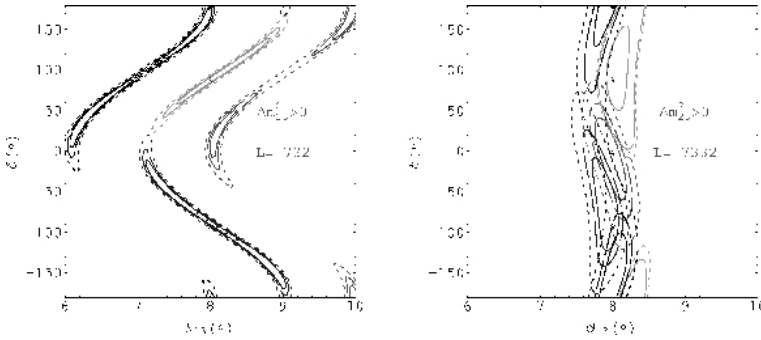


Fig. 5.6: Simultaneous fits of δ and θ_{13} at $L = 732$ km (left) and $L = 7332$ km (right) for different central values of $\bar{\delta} = -90^\circ, 0^\circ, 90^\circ, 180^\circ$ and $\bar{\theta}_{13} = 8^\circ$.

solution is clearly seen for the central value of $\bar{\delta} = 0^\circ$ as an isolated island. For the central values of $\bar{\delta} = -90^\circ$ and $\bar{\delta} = 90^\circ$, the degeneracy is responsible for the rather large contours which encompass the two solutions. As $\bar{\theta}_{13}$ diminishes the fake solution for $\bar{\delta} = 90^\circ$ moves towards $\delta = 180^\circ$, as expected because, in the solar regime, the vacuum fake image lies at $\delta = 180^\circ$.

Figs. 5.6 show the fits for $\bar{\theta}_{13} = 8^\circ$ at $L = 732$ km and 7332 km. In the former, the expected continuous line of solutions of the form given by eq. (5.11) is clearly seen. The measurement of δ is thus impossible at this baseline if θ_{13} is unknown. In the longer baseline, the sensitivity to δ is similarly lost but for a different reason: the CP-signal is fading away (indeed the underlying degenerate solutions become much closer in θ_{13}) and statistics is diminishing.

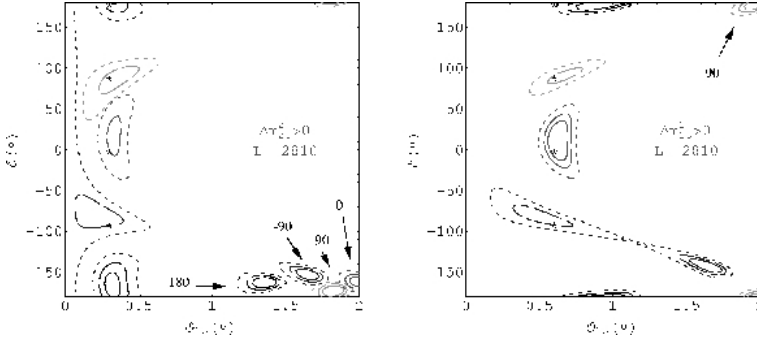


Fig. 5.7: Simultaneous fits of δ and θ_{13} at $L = 2810$ km for different central values of $\bar{\delta} = -90^\circ, 0^\circ, 90^\circ, 180^\circ$ and $\bar{\theta}_{13} = 0.3^\circ$ (left), 0.6° (right). The value of $\bar{\delta}$ for the degenerate solutions is indicated.

Solar Regime

In Fig. 5.7 are shown the fits including efficiencies and backgrounds for $L = 2810$ km for central values of $\bar{\delta} = -90^\circ, 0^\circ, 90^\circ, 180^\circ$ and $\bar{\theta}_{13} = 0.3^\circ$ (left) and $\bar{\theta}_{13} = 0.6^\circ$ (right). On the left, the images of the four points chosen appear grouped at the right/lower side of the figure. These are the solutions that mimic $\theta_{13} = 0$ as predicted from (5.13). The comparison of these figures with Fig. 5.5 illustrate the expected decrease of the sensitivity to CP violation for very small θ_{13} .

5.4 Combinations

As explained in section 5.3.2 on page 53, there exists generically, at a given (anti)neutrino energy and fixed baseline, a second value of the set (θ_{13}, δ) that gives the same oscillation probabilities for neutrinos and antineutrinos as the true value that appears in nature. That's what we call *intrinsic degeneracies*.

It has also been pointed out [21] that other fake solutions might appear from unresolved degeneracies in two other oscillation parameters:

- the sign of Δm_{23}^2
- θ_{23} , upon the exchange $\theta_{23} \leftrightarrow \pi/2 - \theta_{23}$ for $\theta_{23} \neq \pi/4$.

It is not expected that these degeneracies will be resolved before the time of the Superbeam or Neutrino Factory operation. However, the subleading transitions $\nu_e \leftrightarrow \nu_\mu$, from which the parameters θ_{13} and δ can be measured, are sensitive to these discrete ambiguities. A complete analysis of the sensitivity to the set

(θ_{13}, δ) should therefore assume that $\text{sign}(\Delta m_{23}^2)$ can be either positive or negative, and $\theta_{23} >$ or $< \pi/4$. If a wrong choice of these possibilities cannot fit the data, the ambiguities will be resolved, else they will generically give rise to new fake solutions for the parameters θ_{13} and δ .

There are different strategies to eliminate some of the fake solutions. It is possible to make a combination of different baselines [22], an improved experimental technique allowing the measurement of the neutrino energy with good precision [18], the supplementary detection of $\nu_e \rightsquigarrow \nu_\tau$ channels [17] and a cluster of detectors at a superbeam facility located at different off-axis angles, so as to have different $\langle E \rangle$ [20].

All the strategies are based in the inclusion of new information into the analysis, combining the ‘standard Neutrino Factory dataset’ with some other dataset, be it different baselines, energy resolution, new channels or modifications of the flux. We will present what is one of the most promising combinations: a Neutrino Factory with a Superbeam.

5.4.1 Neutrino Factory with Superbeam

The development of a Neutrino Factory requires, by design, the essentials of a Superbeam facility as an intermediate step. Although the ultimate precision and discovery goals in neutrino oscillation physics may only be attained with a neutrino factory from muon storage rings, those “for free” superbeam results can already lead to significant progress in central physics issues, as is the case of the degeneracies.

Superbeams and Neutrino Factory are not alternative options, but successive steps. In this perspective, the analysis strategy is to contemplate the combination of their expected physics results, which would improve the measurements of the neutrino factory and may resolve the problem of degeneracies.

For concreteness, the results of the next sections will consider the following experimental setup: 1) A Neutrino Factory with a parent μ^\pm energy of 50 GeV and two reference baselines at 732 and 2810 km for the Neutrino Factory, and 2) A Superbeam with the proposed CERN SPL accelerator, with an average energy of $\langle E \rangle = 0.25$ GeV and a baseline of 130 km (CERN-Fréjus).

5.4.2 Resolution of Intrinsic Degeneracies

At a fixed neutrino energy and baseline, there are degenerate solutions in the (θ_{13}, δ) plane for fixed values of the oscillation probabilities $\nu_e(\bar{\nu}_e) \rightsquigarrow \nu_\mu(\bar{\nu}_\mu)$. If (θ_{13}, δ) are the values chosen by nature, the conditions

$$\begin{aligned}
P_{\nu_e \nu_\mu}(\theta'_{13}, \delta') &= P_{\nu_e \nu_\mu}(\theta_{13}, \delta) \\
P_{\bar{\nu}_e \bar{\nu}_\mu}(\theta'_{13}, \delta') &= P_{\bar{\nu}_e \bar{\nu}_\mu}(\theta_{13}, \delta)
\end{aligned}
\tag{5.19}$$

can be generically satisfied by another set (θ'_{13}, δ') . Using the approximate formulae of eq. (5.3), it is easy to find the expression for these *intrinsic* degeneracies deep in the atmospheric and solar regimes, as shown in section 5.3.2.

For θ_{13} sufficiently large and in the vacuum approximation, apart from the true solution, $\delta' = \delta$ and $\theta'_{13} = \theta_{13}$, there is a fake one at

$$\begin{aligned}
\delta' &\simeq \pi - \delta \\
\theta'_{13} &\simeq \theta_{13} + \cos \delta \sin 2\theta_{12} \frac{\Delta m_{12}^2 L}{4E} \cot \theta_{23} \cot \frac{\Delta m_{23}^2 L}{4E}
\end{aligned}
\tag{5.20}$$

Note that for values $\delta = -90^\circ, 90^\circ$, the two solutions degenerate into one. Typically $\cot \frac{\Delta m_{23}^2 L}{4E}$ has on average opposite signs for the proposed superbeam and neutrino factory setups, for $\Delta m_{23}^2 = 3 \times 10^{-3} eV^2$:

	$\langle E \rangle$ (GeV)	L (km)	$\cot \frac{\Delta m_{23}^2 L}{4E}$
SB - SPL	0.25	130	-0.43
JHF - off-axis	0.7	295	-0.03
NF@732	30	732	+10.7
NF@2810	30	2810	+2.68
β -beam	0.35	130	+0.17

When $\theta_{13} \rightarrow 0$ and in the vacuum approximation, the intrinsic degeneracy is independent of δ :

$$\begin{aligned}
&\left\{ \begin{array}{l} \text{if } \cot \left(\frac{\Delta m_{23}^2 L}{4E} \right) > 0 \text{ then } \delta' \simeq \pi \\ \text{if } \cot \left(\frac{\Delta m_{23}^2 L}{4E} \right) < 0 \text{ then } \delta' \simeq 0 \end{array} \right\} \\
\theta'_{13} &\simeq \sin 2\theta_{12} \frac{\Delta m_{12}^2 L}{4E} \left| \cot \theta_{23} \cot \left(\frac{\Delta m_{23}^2 L}{4E} \right) \right|
\end{aligned}
\tag{5.21}$$

This solution is named $\theta_{13} = 0$ -mimicking solution and occurs because there is a value of θ'_{13} for which there is an exact cancellation of the atmospheric and interference terms in both the neutrino and antineutrino probabilities simultaneously, with $\sin \delta' = 0$.

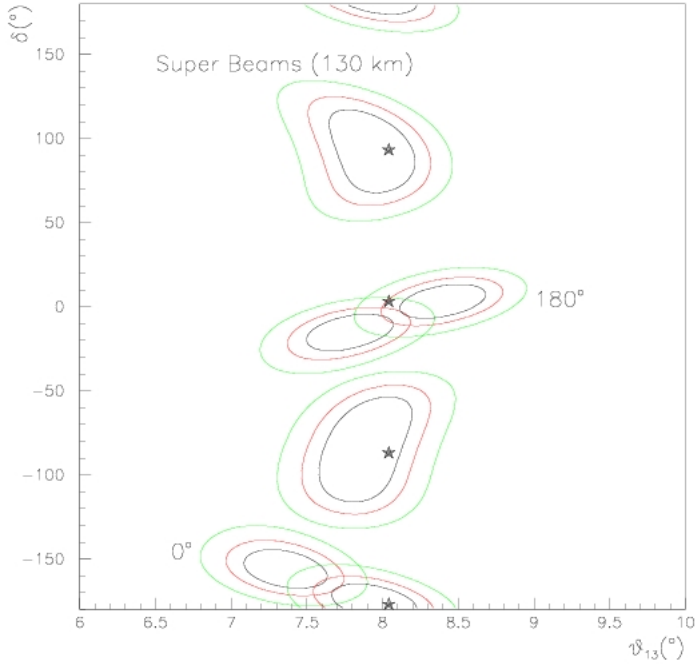


Fig. 5.8: Fits to the given true solutions and their intrinsic degenerate solutions at a Super-beam facility. The 68.5%, 90% and 99% contours are depicted, for four central values of $\delta = -90^\circ, 0^\circ, 90^\circ, 180^\circ$ and $\theta_{13} = 8^\circ$.

Figure 5.8 shows the results of measuring (θ_{13}, δ) at the SPL-superbeam facility, for $\theta_{13} = 8^\circ$ and the central values of $\delta = -180^\circ, -90^\circ, 90^\circ, 180^\circ$. The intrinsic degeneracies clearly appear and are well described by eqs. (5.20).

The analysis is based on the total number of electron/positron events, so it is not assumed that the neutrino energy can be reconstructed.

A comparison of the Neutrino Factory and SPL-superbeam fits shows that the displacement of the fake solution with respect to the true one is opposite for the two facilities.

In order to understand the intermediate region between the solar and atmospheric regimes, as well as the influence of matter effects, the possible physical solutions to eqs. (5.19) can be computed numerically, using the approximate formulae for the probabilities including matter effects. In what follows, L and E are fixed to the average values for the different facilities. The results for the shift

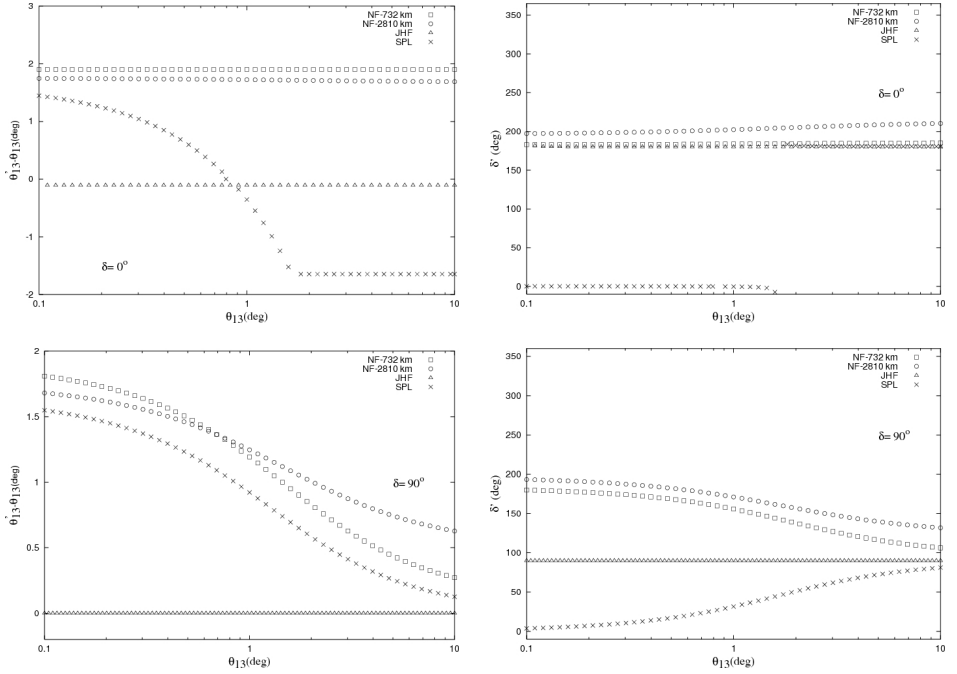


Fig. 5.9: $\theta'_{13} - \theta_{13}$ (left) an δ' (right) versus θ_{13} , for the intrinsic fake solution, for fixed values of $\delta = 0^\circ$ (up) and $\delta = 90^\circ$ (down).

$\theta'_{13} - \theta_{13}$ and δ' are shown in Fig. 5.9 as a function of θ_{13} , for two values of $\delta = 0^\circ, 90^\circ$ and for the different experimental setups. In the whole range of parameters there are two solutions, as expected by periodicity in δ , since one solution is warranted: the true one.

The most important point to note in eqs. (5.20) and (5.21) and in Figs. 5.9 is that the position (measured in $\theta'_{13} - \theta_{13}$ or δ') of the degenerate solution is very different in the neutrino factory, the SPL-superbeam and JHF setups. As a result, it is expected that any combination of the results of two of these three facilities could in principle exclude the fake solutions. The $\theta'_{13} - \theta_{13}$ of the fake solution depends strongly on the baseline and the neutrino energy through the ratio L/E , so the combination of the results of two experiments with a different value for this ratio should be able to resolve these degeneracies, within their range of sensitivity. Even more important is that, for small θ_{13} , δ' may differ by 180° if the two facilities have opposite sign for $\cot \frac{\Delta m_{23}^2 L}{4E}$. For the Neutrino Factory setups, this sign is clearly positive, since the measurement of CP violation requires, because of the

large matter effects, a baseline considerably shorter than that corresponding to the maximum of the atmospheric oscillation (in vacuum), where the cotangent changes sign. In the superbeams scenario, on the other hand, because of the smaller $\langle E \rangle$, matter effects are small at the maximum of the atmospheric oscillation, which then becomes the optimal baseline for CP violation studies. It is then not very difficult to ensure that $\cot \frac{\Delta m_{23}^2 L}{4E}$ be dominantly negative in this case, which results in an optimal complementarity of the two facilities in resolving degeneracies.

Effect of Δm_{23}^2

Clearly the position of the fake solution is very sensitive to the atmospheric $|\Delta m_{23}^2|$. In matter we expect a milder dependence, especially if matter effects become dominant. In Fig. 5.10 one can see the separation in θ_{13} of the intrinsic degenerate solution at $\delta = 0^\circ$ in the atmospheric regime as a function of $|\Delta m_{23}^2|$. Although in general the separation becomes smaller for smaller $|\Delta m_{23}^2|$, it is sizeable in the whole allowed range. The relative difference between the results for the neutrino factory and the SPL superbeam option is always largest, although the differences between the two superbeams and that between the neutrino factory and JHF are also very large. Note also that the sign of $\theta'_{13} - \theta_{13}$, which is related to that of $\cot \frac{\Delta m_{23}^2 L}{4E}$, is positive in all the domain for the neutrino factory baselines and negative in most of the domain for SPL-superbeam scenario, which implies that the difference in δ' between the two facilities is 180° for small θ_{13} . For JHF, is negative only for $|\Delta m_{23}^2| \geq 3 \times 10^{-3} eV^2$.

Concerning the dependence on the solar parameters, it enters only through the combination of $\sin 2\theta_{12} \frac{\Delta m_{12}^2 L}{4E}$. In general $\theta'_{13} - \theta_{13}$ is linear in this quantity, so degenerate solutions become closer with smaller Δm_{12}^2 and also closer to the true solution. Note however that δ' in the solar regime does not depend on the solar parameters and that it differs by 180° in the two facilities, and this separation will remain when Δm_{12}^2 is lowered.

Effect of Δm_{12}^2

Turning to the variation of the solar parameters while in the atmospheric regime, we will see that, if the two facilities that are combined have opposite $\text{sign}(\cot \frac{\Delta m_{23}^2 L}{4E})$, the effect of lowering Δm_{12}^2 is not dramatic either in the resolution of degeneracies. The statistical error on the measurement of θ_{13} and δ is mainly independent of the solar parameters (it is dominated by the atmospheric term), which means that at some point when Δm_{12}^2 is lowered, the degenerate solutions of the two facilities will merge, since the error remains constant while the separation of the solutions

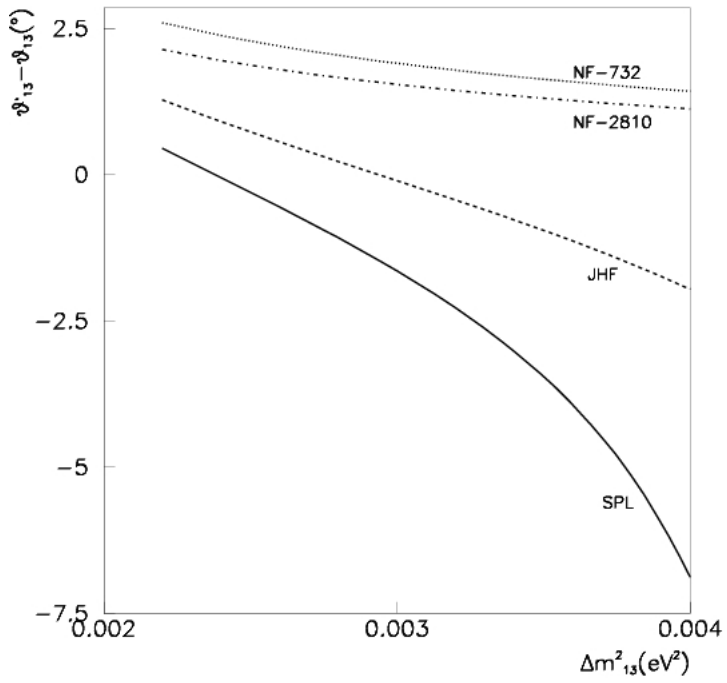


Fig. 5.10: $\theta'_{13} - \theta_{13}$ versus $|\Delta m^2_{23}|$ for the intrinsic fake solution in the atmospheric regime and $\delta = 0^\circ$.

get smaller. However, because of the opposite sign of $\theta'_{13} - \theta_{13}$, the solutions of the two facilities will merge only when they merge with the true solution in θ_{13} . If this happens, it would therefore not bias the measurement of θ_{13} and δ .

The combination of a Neutrino Factory with the SPL-superbeam facility, for the optimal Neutrino Factory baseline $L = 2810$ km, is sufficient to get rid of all the fake solutions, as shown in the result of a complete numerical analysis in Figs. 5.11 (left). It is to note that indeed the disappearance of the fake solutions takes place even in the solar regime.

There are some differences when the combination of the SPL-Superbeam is done with a shorter Neutrino Factory baseline of $L = 732$ km. The degenerate solution is not so relevant to this neutrino factory baseline when considered alone, because there the sensitivity to CP violation is so poor that there exists a continuum of almost degenerate solutions, which makes the determination of δ impossible with the wrong-sign muon signals. The combination of the results from this neutrino factory baseline with those from the SPL-superbeam facility is summarized in Figs. 5.11 (right). Not only do the fake solutions corresponding to the intrinsic degeneracies in the superbeam disappear, but the accuracy in the determination of the true solution becomes competitive with that obtained in the combination with the optimal baseline for large values of θ_{13} . At small values of θ_{13} the latter still gives better results, as expected.

5.4.3 $\text{sign}(\Delta m_{23}^2)$ Degeneracy

To see the effect of $\text{sign}(\Delta m_{23}^2)$ one can try to perform the analysis assuming its value is the opposite of the real one. The oscillation probability with the sign of Δm_{23}^2 reversed will be called $P'_{\nu_e\nu_\mu(\bar{\nu}_e\bar{\nu}_\mu)}(\theta_{13}, \delta)$. New fake solutions (θ'_{13}, δ') , at fixed E_ν and L , will appear if the equations

$$\begin{aligned} P'_{\nu_e\nu_\mu}(\theta'_{13}, \delta') &= P_{\nu_e\nu_\mu}(\theta_{13}, \delta) \\ P'_{\bar{\nu}_e\bar{\nu}_\mu}(\theta'_{13}, \delta') &= P_{\bar{\nu}_e\bar{\nu}_\mu}(\theta_{13}, \delta) \end{aligned} \quad (5.22)$$

have solutions in the allowed physical range.

It turns out that there are generically two fake solutions to eqs. (5.22). It is very easy to find them in the vacuum approximation, as the mirror the two solutions (true and fake) obtained in the analysis of the intrinsic degeneracies. It can be seen in eq. (5.3) that a change in the sign of Δm_{23}^2 can be traded in vacuum by the substitution $\delta \rightarrow \pi - \delta$, implying the for eqs. (5.22)

$$P'_{\nu_e\nu_\mu(\bar{\nu}_e\bar{\nu}_\mu)}(\theta'_{13}, \delta') \simeq P_{\nu_e\nu_\mu(\bar{\nu}_e\bar{\nu}_\mu)}(\theta'_{13}, \pi - \delta') \quad (5.23)$$

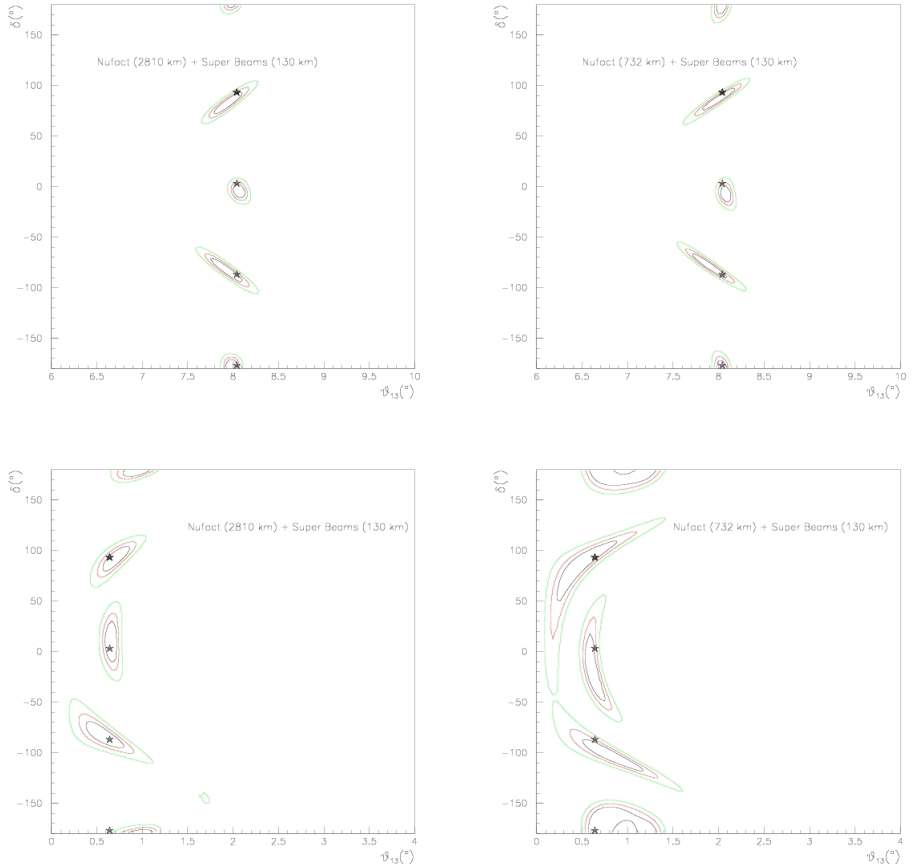


Fig. 5.11: Fits combining the results from the SPL-Superbeam facility and a Neutrino Factory baseline at $L = 2810$ km (left) or $L = 732$ km (right). The true values illustrated correspond to $\delta = -90^\circ, 0^\circ, 90^\circ, 180^\circ$ and $\theta_{13} = 8^\circ$ (top) or $\theta_{13} = 0.6^\circ$ (bottom). The fake intrinsic solutions completely disappear in the combinations.

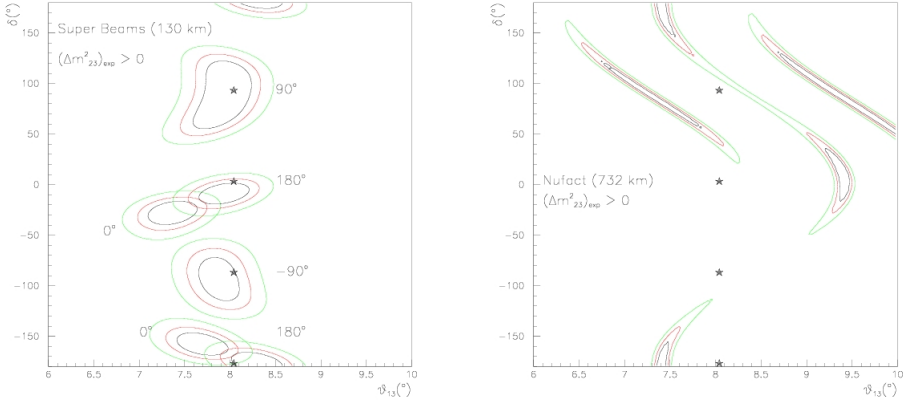


Fig. 5.12: Fits for central values $\theta_{13} = 8^\circ$ and $\delta = -90^\circ, 0^\circ, 90^\circ, 180^\circ$ for the SPL-Superbeam (left) and Neutrino Factory at $L = 732$ km (right). The real sign for Δm_{23}^2 is assumed to be positive, while the fits are performed with the opposite sign. All fake solutions disappear when the two sets of data are combined.

in the vacuum approximation. Consequently, the solutions in vacuum can be obtained from those present for the intrinsic case, upon the substitution $\delta' \rightarrow \pi - \delta'$. One of them mirrors the true (nature) solution and will be called below solution I, given in vacuum by

$$\begin{aligned}\delta' &\simeq \pi - \delta \\ \theta'_{13} &\simeq \theta_{13}\end{aligned}\tag{5.24}$$

The fact that it is approximately E and L -independent suggests that it will be hard to eliminate it by exploiting the L , E dependence of different facilities, as indeed is confirmed by the fits below. Fortunately, this fake solution does not interfere significantly with the determination of θ_{13} or CP-violation (i. e. $\sin \delta$).

The second fake sign solution, which will be called solution II, can be read in vacuum from eqs. (5.20) and (5.21), upon the mentioned $\delta' \rightarrow \pi - \delta'$ exchange. It is strongly L - and E -dependent. Both solutions I and II can be seen in the numerical analysis for the SPL superbeam in Fig. 5.12 (left), for $\theta_{13} = 8^\circ$ and positive $\text{sign}(\Delta m_{23}^2)$.

Matter effects are obviously very important in resolving fake sign solutions: the task should thus be easier at large θ_{13} and large enough neutrino factory baselines, where matter effects are largest. In fact it is easy to prove that no solutions

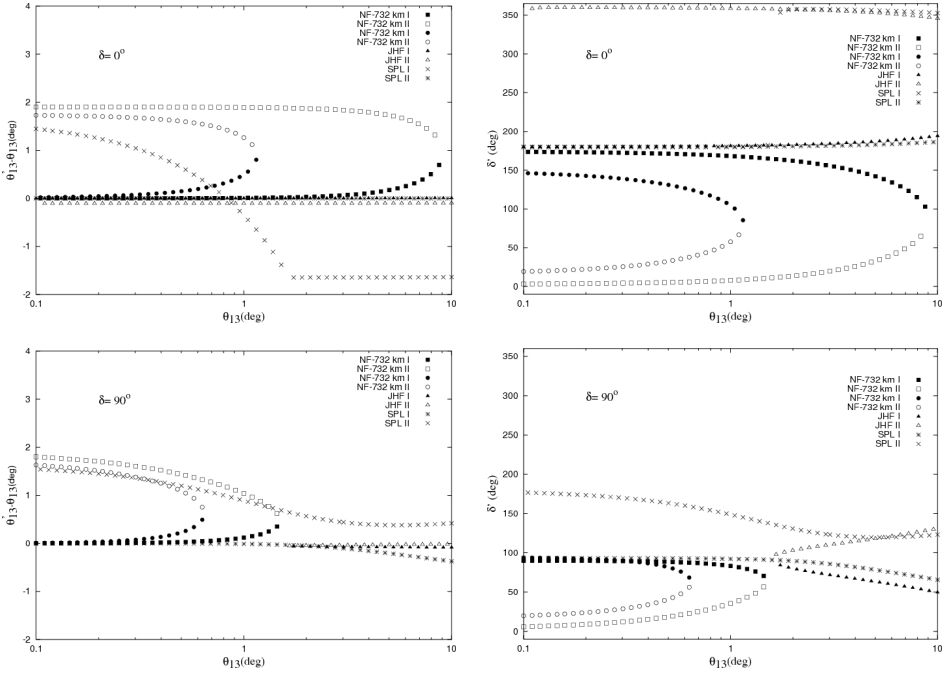


Fig. 5.13: $\theta'_{13} - \theta_{13}$ (left) and δ' (right) for the sign degeneracies as functions of θ_{13} for fixed values of $\delta = 0^\circ$ (up) and $\delta = 90^\circ$ (down).

can remain for large enough θ_{13} . This can be seen in Figs. 5.13, which show the fake sign solutions as they result from solving numerically eqs. (5.22) (using the approximate probabilities with matter effects included) for the different experiments. For small θ_{13} the two solutions I and II exist in all cases, while for large θ_{13} they degenerate and disappear because of matter effects. Nevertheless even if no fake solution exists, there might be approximate ones that will show up in a measurement with finite errors.

A numerical analysis with fits including realistic background errors and efficiencies confirm the above expectations, at each given facility. There is no fake sign solutions for values of $\theta_{13} > 2^\circ$, when considering just one neutrino factory baseline of $L = 2810$ km (or longer), while for $2^\circ > \theta_{13} > 1^\circ$ they do appear but get eliminated when the data are combined with those from the SPL Superbeam. At $L = 732$ km some fake sign solutions remain close to the present experimental limit for θ_{13} , as shown in Figs. 5.12 (right). Once again, in the combination of these latter data with those from the SPL superbeam facility, all fake sign solutions disappear for large $\theta_{13} \geq 4^\circ$, and the sign of Δm_{23}^2 could thus be determined from

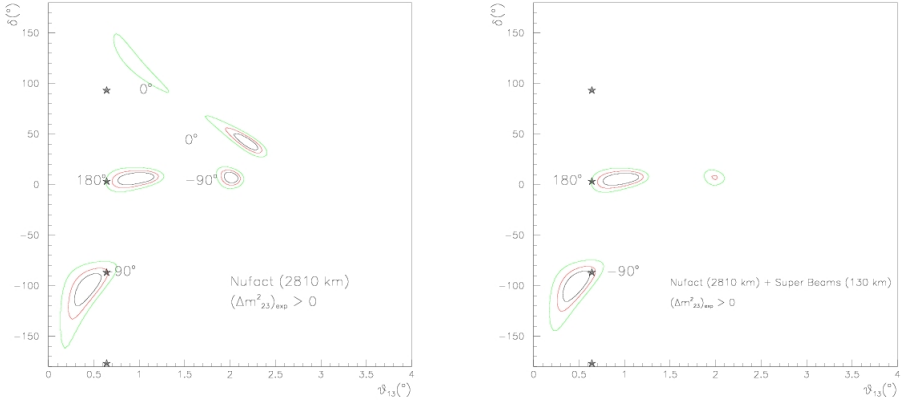


Fig. 5.14: Fits resulting in fake sign solutions, for central values $\theta_{13} = 0.6^\circ$ and $\delta = -90^\circ, 0^\circ, 90^\circ, 180^\circ$. The real sign for Δm_{23}^2 is positive, while the fits are performed with the opposite sign. The results from a Neutrino Factory baseline at $L = 2810$ km can be appreciated on the left, while their combination with data from the SPL-Superbeam can be seen on the right.

it.

Figures 5.13 also illustrate that solution I is more facility-independent than solution II, as argued above. The solutions that survive in the combinations for small θ_{13} are indeed of type I, as shown in Figs. 5.14.

In conclusion, the sign of Δm_{23}^2 can be determined from data at an intermediate or long neutrino factory baseline alone for θ_{13} well inside the atmospheric regime. For the larger values of θ_{13} , the combination of data from the superbeam facility and a $L = 732$ m neutrino factory baseline also results in no fake sign solutions.

With lowering θ_{13} ($\theta_{13} > 1^\circ$ for our central parameters), the sign can still be determined through the combination of superbeam and neutrino factory data at the intermediate or long distance.

Finally, for the range $\theta_{13} < 1^\circ$, the sign cannot be determined, but the combination of data from the superbeam facility and an intermediate (or long) neutrino factory baseline is still important to reduce the fake solutions to those of type I, which do not interfere significantly with the determination of θ_{13} and δ .

Concerning the dependence on the solar parameters, it is not expected that the conclusions will change very much with lower $\sin 2\theta_{12}\Delta m_{12}^2$. The argument for solutions of type II parallels that given in the previous subsection for the intrinsic fake solution, while the existence and position of the type I solutions is pretty

insensitive to the solar parameters.

5.4.4 $\theta_{23} \rightarrow \pi/2 - \theta_{23}$ Degeneracy

The present atmospheric data indicate that θ_{23} is close to maximal, although not necessarily 45° . Super-Kamiokande results give 90% CL-allowed parameter regions for $\sin^2 2\theta_{23} > 0.88$, translating into the allowed range $35^\circ < \theta_{23} < 55^\circ$. Therefore even if the value of $\sin^2 2\theta_{23}$ is determined with great accuracy in disappearance measurements, there may remain a discrete ambiguity under the interchange $\theta_{23} \leftrightarrow \pi/2 - \theta_{23}$. If this θ_{23} ambiguity is not cleared up by the time of the neutrino factory operation, supplementary fake solutions may appear when extracting θ_{13} and δ , when the wrong choice of octant is taken for θ_{23} . Fake solutions follow from solving the system of equations, for fixed L and E_ν :

$$\begin{aligned} P''_{\nu_e\nu_\mu}(\theta'_{13}, \delta') &= P_{\nu_e\nu_\mu}(\theta_{13}, \delta) \\ P''_{\bar{\nu}_e\bar{\nu}_\mu}(\theta'_{13}, \delta') &= P_{\bar{\nu}_e\bar{\nu}_\mu}(\theta_{13}, \delta) \end{aligned} \quad (5.25)$$

where $P''_{\bar{\nu}_e\bar{\nu}_\mu}$ denotes the oscillation probabilities on the exchange $\theta_{23} \rightarrow \pi/2 - \theta_{23}$.

It turns out that, within the allowed range for the parameters, there are generically two solutions to these equations. They should converge towards the true solutions and its intrinsic degeneracy, in the limit $\theta_{23} \rightarrow \pi/4$. It is called again solution I that which mirrors nature's choice and solution II that which mirrors the intrinsic degeneracy. Because of this parenthood, solution I is a priori expected to present generically less L and E dependence than solution II, and be thus more difficult to eliminate in the combination.

It is easy and simple to obtain the analytical form of the fake degeneracies in the vacuum approximation, in which, from eqs. (5.3) we get

$$\begin{aligned} P''_{\nu_e\nu_\mu(\bar{\nu}_e\bar{\nu}_\mu)}(\theta'_{13}, \delta') &= c_{23}^2 \sin^2 2\theta'_{13} \sin^2 \frac{\Delta m_{23}^2 L}{4E} \\ &+ s_{23}^2 \sin^2 2\theta_{12} \sin^2 \frac{\Delta m_{12}^2 L}{4E} \\ &+ J' \cos\left(\delta' \mp \frac{\Delta m_{23}^2 L}{4E}\right) \frac{\Delta m_{12}^2 L}{4E} \sin\left(\frac{\Delta m_{23}^2 L}{4E}\right) \end{aligned} \quad (5.26)$$

Atmospheric Regime

For large θ_{13} , fake θ_{23} solutions are given by

$$\begin{aligned}
\sin \delta' &\simeq \cot \theta_{23} \sin \delta \\
\theta'_{13} &\simeq \tan \theta_{23} \theta_{13} \\
&+ \frac{\sin 2\theta_{12} \frac{\Delta m_{12}^2 L}{4E}}{2 \sin \frac{\Delta m_{23}^2 L}{4E}} \left(\cos \left(\delta - \frac{\Delta m_{23}^2 L}{4E} \right) - \tan \theta_{23} \cos \left(\delta' - \frac{\Delta m_{23}^2 L}{4E} \right) \right)
\end{aligned} \tag{5.27}$$

This system describes two solutions. For one of them (I) the L - and E -dependent terms in eqs. (5.27) tend to cancel for $\theta_{23} \rightarrow \pi/4$, resulting in $\theta'_{13} = \theta_{13}$, $\delta' = \delta$ in this limit. The other solution (II) coincides in this limit with that for the intrinsic degeneracy, eq. (5.20), as expected. For both fake θ_{23} solutions, deep in the atmospheric regime the shift $\theta'_{13} - \theta_{13}$ is positive (negative) for $\theta_{23} > (<)\pi/4$. Also, from eqs. (5.27), no fake solutions are expected for $\|\cot \theta_{23} \sin \delta\| > 1$. In the plots of Figs. 5.15 and 5.16 are the solutions to eqs. (5.25), including matter effects, for θ_{23} at the two extremes of the 90% CL-allowed interval. It is to note that for large θ_{13} there is one solution (I) that is more facility-independent than the other, although the E, L dependence is sizeable for both solutions (see for instance the curves for $\delta = 90^\circ$ in figs. 5.16) when θ_{23} is so far from maximal.

The fits with the wrong choice of octant for θ_{23} and central values of θ_{23} at the limit of the currently allowed domains, confirm the expectations above and indicate a situation close to that for the fake sign degeneracies, albeit slightly more difficult. For instance, at the $L = 2810$ km baseline of the neutrino factory alone, still some fake θ_{23} solutions remain down to $\theta_{13} > 2^\circ$, but again they all disappear when combined with the SPL superbeam data. As an illustration, in Figs. 5.17 are the results for $\theta_{23} = 35^\circ$ and $\theta_{13} = 4^\circ$, at the SPL Superbeam facility (left) and the $L = 2810$ km Neutrino Factory baseline (right). The same exercise but for an $L = 732$ km baseline of the neutrino factory, results in the elimination of the θ_{23} degeneracies only for $\theta_{13} \geq 8^\circ$.

Solar Regime

For $\theta_{13} \rightarrow 0^\circ$, there are again two fake solutions if the following condition is met:

$$\tan^2 \theta_{23} < \frac{1}{\sin^2 \frac{\Delta m_{23}^2 L}{4E}} \tag{5.28}$$

Otherwise no solution exists. This is important for the larger possible values of θ_{23} and well reflected in Figs. 5.16, which show the exact solutions for $\theta_{23} = 55^\circ$. Indeed no fake θ_{23} degeneracies appear in the superbeam facilities in this case, for θ_{13} in the solar regime.

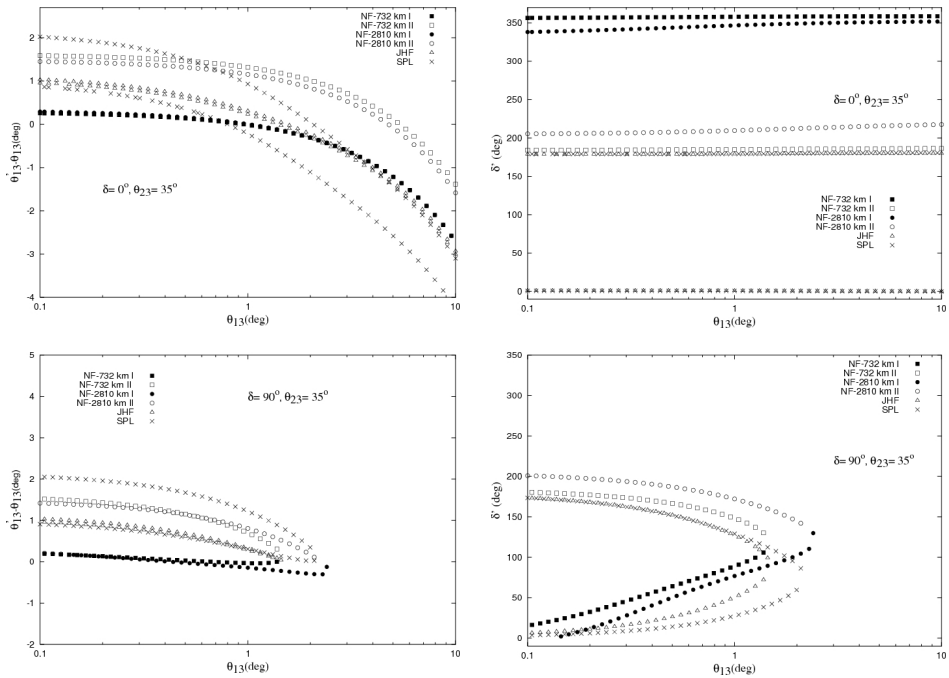


Fig. 5.15: $\theta'_{13} - \theta_{13}$ (left) and δ' (right) for the θ_{23} fake solution as functions of θ_{13} , for $\theta_{23} = 35^\circ$, for fixed values of $\delta = 0^\circ$ (up) and $\delta = 90^\circ$ (down).

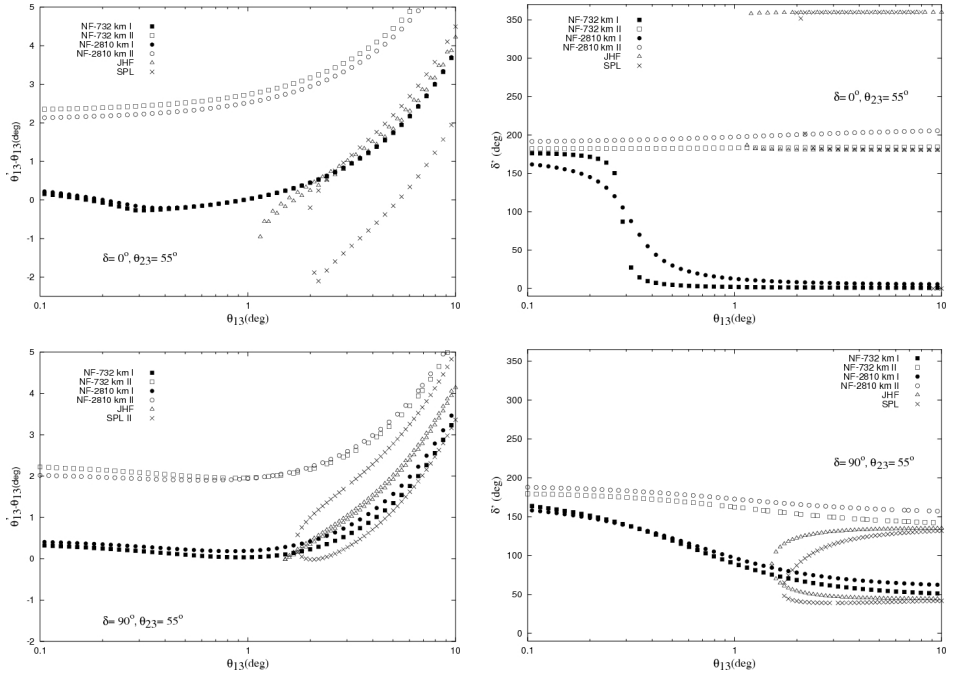


Fig. 5.16: $\theta'_{13} - \theta_{13}$ (left) and δ' (right) for the θ_{23} fake solution as functions of θ_{13} , for $\theta_{23} = 55^\circ$, for fixed values of $\delta = 0^\circ$ (up) and $\delta = 90^\circ$ (down).

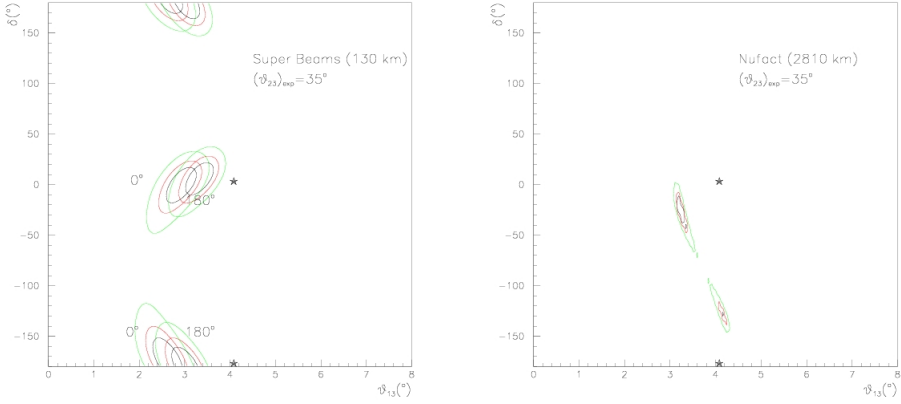


Fig. 5.17: Fake solutions due to θ_{23} degeneracies for SPL-Superbeam results (left) and a $L = 2810$ km Neutrino Factory baseline (right), for $\theta_{23} = 35^\circ$, $\theta_{13} = 4^\circ$ and $\delta = -90^\circ, 0^\circ, 90^\circ, 180^\circ$. The combination of the results from both experiments resolves the degeneracies.

For $\theta_{13} \rightarrow 0^\circ$, eqs. (5.25) can be solved to first order in $\epsilon_{23} \equiv \tan \theta_{23} - 1$. Solution I becomes in this limit:

$$\left\{ \begin{array}{l} \text{if } \cos 2\theta_{23} \cot \left(\frac{\Delta m_{23}^2 L}{4E} \right) > 0 \text{ then } \delta' \simeq 0 \\ \text{if } \cos 2\theta_{23} \cot \left(\frac{\Delta m_{23}^2 L}{4E} \right) < 0 \text{ then } \delta' \simeq \pi \end{array} \right\}$$

$$\theta'_{13} \simeq \sin 2\theta_{12} \frac{\Delta m_{12}^2 L}{4E} \left| \epsilon_{23} \csc \left(\frac{\Delta m_{23}^2 L}{2E} \right) \right| \quad (5.29)$$

Similarly, solution II for $\theta_{13} \rightarrow 0^\circ$ is given by:

$$\left\{ \begin{array}{l} \text{if } \cot \left(\frac{\Delta m_{23}^2 L}{4E} \right) > 0 \text{ then } \delta' \simeq \pi \\ \text{if } \cot \left(\frac{\Delta m_{23}^2 L}{4E} \right) < 0 \text{ then } \delta' \simeq 0 \end{array} \right\}$$

$$\theta'_{13} \simeq \sin 2\theta_{12} \frac{\Delta m_{12}^2 L}{4E} \left(\left| \cot \frac{\Delta m_{23}^2 L}{4E} \right| \pm \epsilon_{23} \cot \frac{\Delta m_{23}^2 L}{2E} \right) \quad (5.30)$$

where the sign \pm corresponds to the sign($\cot \frac{\Delta m_{23}^2 L}{4E}$). The intrinsic degeneracy, eq. (5.21), is recovered for $\theta_{23} = 45^\circ$. Note that, in the solar regime both fake

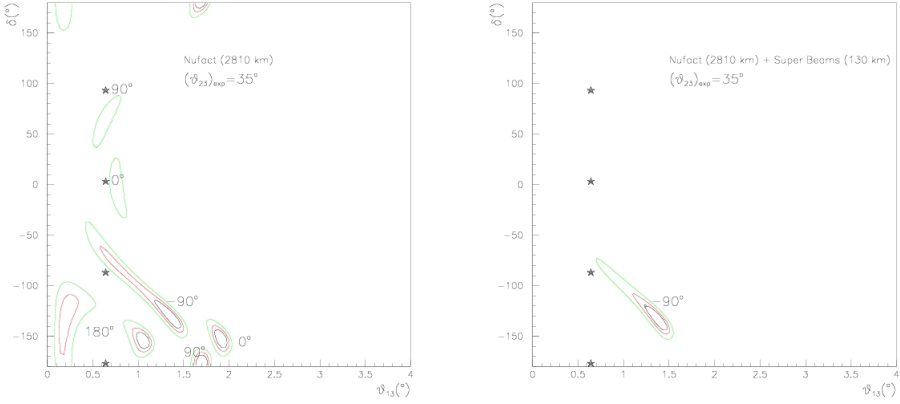


Fig. 5.18: Fake solutions due to θ_{23} degeneracies for a $L = 2810$ km Neutrino Factory baseline (left) and its combination with a SPL-Superbeam (right). The central values are $\theta_{13} = 0.6^\circ$ and $\delta = -90^\circ, 0^\circ, 90^\circ, 180^\circ$. The nature θ_{23} is $< 45^\circ$, while the fits have been performed with $\theta_{23} > 45^\circ$.

θ_{23} solutions have a sizeable L , E dependence, when θ_{23} is far from maximal. These two solutions can be seen in Figs. 5.15 and 5.16 for small θ_{13} . Only for the neutrino factory setups do solutions I and II remain on the same curve in the solar and atmospheric regimes. In the case of the SPL and JHF facilities, they are mixed.

Figures 5.18 show the fits for $\theta_{13} = 0.6^\circ$, for a Neutrino Factory at $L = 2810$ km (left) as well as the same combined with the results from the SPL superbeam facility (right): only one fake solution remains in the latter, which results from the merging of solution I for superbeams and solution II for the neutrino factory, owing to the finite resolution.

In general, the Neutrino Factory and SPL-Superbeam combination brings an enormous improvement to the solution of these fake degeneracies, particularly for large θ_{13} . The conclusions are rather parallel to those for the fake $\text{sign}(\Delta m_{23}^2)$ solutions, with the caveat that for the θ_{23} ambiguities, solution I, which is harder to resolve, is not that close to satisfying $\sin \delta' = \sin \delta$, and it is thus potentially more harmful to the measurement of CP violation.

As regards the dependence on the solar parameters, the arguments of the previous two subsections can be repeated for solutions I and II, when θ_{23} is close to maximal. When θ_{23} is farther from $\pi/4$, the situation is more confusing since both solutions have a dependence on the solar parameters and a detailed exploration of the whole LMA parameter space is necessary.

5.4.5 The Silver Channels

Resolving Intrinsic Degeneracies

One possibility that can help very much to remove degeneracies further is to measure also the $\nu_e \rightsquigarrow \nu_\tau$ and $\bar{\nu}_e \rightsquigarrow \bar{\nu}_\tau$ transition probabilities. The relevance of these *silver* channels in reducing intrinsic degeneracies was studied in ref. [17], in the atmospheric regime. The approximate oscillation probabilities in vacuum for $\nu_e \rightsquigarrow \nu_\tau$ ($\bar{\nu}_e \rightsquigarrow \bar{\nu}_\tau$) are:

$$\begin{aligned}
 P_{\nu_e \nu_\tau (\bar{\nu}_e \bar{\nu}_\tau)} &= c_{23}^2 \sin^2 2\theta_{13} \sin^2 \left(\frac{\Delta m_{23}^2 L}{4E} \right) + s_{23}^2 \sin^2 2\theta_{12} \left(\frac{\Delta m_{12}^2 L}{4E} \right)^2 \\
 &- J \cos \left(\pm \delta - \frac{\Delta m_{23}^2 L}{4E} \right) \frac{\Delta m_{12}^2 L}{4E} \sin \frac{\Delta m_{23}^2 L}{4E} \quad (5.31)
 \end{aligned}$$

They differ from those in eq. (5.3) by the interchange $\theta_{23} \rightarrow \pi/2 - \theta_{23}$ and by a change in the sign of the interference term.

For the intrinsic degeneracies in the atmospheric regime, it follows that the sign of $\theta'_{13} - \theta_{13}$ will be opposite to that for the golden $\nu_e \leftrightarrow \nu_\mu$ ($\bar{\nu}_e \leftrightarrow \bar{\nu}_\mu$) channels given in eqs. (5.20). In the solar regime, the intrinsic solutions in these silver channels will thus be identical to eqs. (5.21) upon exchanging $\delta' = 0$ and π , and the combination of the golden and silver channels remains a promising option.

Resolving Fake θ_{23} Solutions

When considering only $\nu_e \rightsquigarrow \nu_\tau$ and $\bar{\nu}_e \rightsquigarrow \bar{\nu}_\tau$ oscillations, the location of the fake solutions related to the θ_{23} ambiguity, in the atmospheric regime, is

$$\begin{aligned}
 \sin \delta' &\simeq \tan \theta_{23} \sin \delta \\
 \theta'_{13} &\simeq \cot \theta_{23} \theta_{13} \\
 &- \sin 2\theta_{12} \frac{\frac{\Delta m_{12}^2 L}{4E}}{2 \sin \frac{\Delta m_{23}^2 L}{4E}} \left(\cos \left(\delta - \frac{\Delta m_{23}^2 L}{4E} \right) - \cot \theta_{23} \cos \left(\delta' - \frac{\Delta m_{23}^2 L}{4E} \right) \right) \quad (5.32)
 \end{aligned}$$

Thus the shift $\theta'_{13} - \theta_{13}$ at large θ_{13} would have the opposite sign to that in eq. (5.27).

In the solar regime, on the other hand, solution I for the ν_τ appearance measurement is the same as that in eq. (5.29), while solution II is different, namely:

$$\theta'_{13} \simeq \sin 2\theta_{12} \frac{\Delta m_{23}^2 L}{4E} \left(\left| \cot \frac{\Delta m_{23}^2 L}{4E} \right| \mp \epsilon_{23} \cot \frac{\Delta m_{23}^2 L}{4E} \right) \quad (5.33)$$

$$\begin{cases} \text{if } \cot \left(\frac{\Delta m_{23}^2 L}{4E} \right) > 0 & \text{then } \delta' \simeq 0 \\ \text{if } \cot \left(\frac{\Delta m_{23}^2 L}{4E} \right) < 0 & \text{then } \delta' \simeq \pi \end{cases}$$

The condition for the existence of solutions in the solar regime is also different:

$$\cot^2 \theta_{23} < \frac{1}{\sin^2 \left(\frac{\Delta m_{23}^2 L}{4E} \right)} \quad (5.34)$$

A detailed analysis for a realistic experimental setup is being done now, but it is expected that the combination of the two appearance measurements $\nu_e \rightsquigarrow \nu_\mu$ and $\nu_e \rightsquigarrow \nu_\tau$ for both polarities can help to resolve the dangerous solution I associated with the θ_{23} ambiguity, for θ_{13} in the atmospheric regime.

Finally, we recall that the disappearance measurements (e. g. $\nu_\mu \rightsquigarrow \nu_\mu$) should also be helpful in reducing these ambiguities for large θ_{23} . If the angle θ_{23} will turn out to be close to maximal (as the best-fit point now indicates), the θ_{23} degeneracies will be of very little relevance.

Resolving Fake $\text{sign}(\Delta m_{23}^2)$ Solutions

As for the removal of the fake $\text{sign}(\Delta m_{23}^2)$ degeneracies, the silver channels will also help, for qualitatively the same reason as in the combination of facilities with opposite value of $\cot \frac{\theta_{13} L}{4E}$. For maximal θ_{23} , the solution of type I in the silver channel is the same in vacuum as that in the golden $\nu_\mu \leftrightarrow \nu_e$ channel, and it is thus not expected to disappear in the combination of the two appearance measurements. The solution of type II, instead, has an opposite displacement in θ_{13} in the atmospheric regime and a difference of 180° in the phase in the solar one.

6. CONCLUSION

A Neutrino Factory from muon storage rings, with muon energies of a few dozen GeV, is an appropriate facility to discover leptonic CP violation through wrong sign muon searches.

At the hypothetical time of the Neutrino Factory, the value of the parameters θ_{13} and δ may be still unknown and will have to be simultaneously measured.

The extraction of a given set of nature values (θ_{13}, δ) results generically in that the true solution may come out accompanied by fake ones, which might interfere severely with the measurement of CP violation. One of the fake solutions comes from the intrinsic correlation between δ and θ_{13} . The others come from the discrete ambiguities: $\text{sign}(\Delta m_{23}^2)$ and $\text{sign}(\cos 2\theta_{23})$.

There is an enormous potential to eliminate these degeneracies in combining the data from a superbeam facility and a neutrino factory. Because of the sizeable matter effects, neutrino factory baselines that are optimal to measure CP violation (as well as shorter ones), imply a considerably smaller ratio L/E than in the proposed superbeam facilities. It turns out that the location of the fake solutions is very sensitive to this quantity, hence the potential of combining the results from both type of facilities.

For θ_{13} near its present limit, the combination of the SPL superbeam data and those from a short neutrino factory baseline ($L = 732$ km) is sufficient to resolve all of them and deliver a clean measurement of θ_{13} and leptonic CP violation. With lowering θ_{13} but still in the atmospheric regime, although the same setup often produces interesting results, it is necessary to consider an intermediate neutrino factory baseline ($L = 2810$ km), together with the superbeam. In particular, the sign of Δm_{23}^2 can be measured from the combination of their data down to $\theta_{13} > 1^\circ$.

For values of $0.5^\circ < \theta_{13} < 1^\circ$ most degeneracies still disappear in the combined data from the SPL superbeam facility and the $L = 2810$ km neutrino factory baseline, but some fake solutions remain, mainly of type I. While those associated to the $\text{sign}(\frac{\Delta m_{23}^2 L}{4E})$ ambiguity bias only slightly the extraction of the true θ_{13} and δ values, those related to θ_{23} would remain a problem, if θ_{23} were far from maximal.

A simultaneous error on the assumed $\text{sign}(\Delta m_{23}^2)$ and θ_{23} octant, gives rise

to additional combined fake solutions: those get resolved when the corresponding individual degeneracies get resolved.

Superbeams and the Neutrino Factory are two successive steps in the same path towards the discovery of leptonic CP violation: a golden path, not so much for its budgetary cost, but for the solid and shining perspective offered by the combination of their physics results.

7. ACKNOWLEDGEMENTS

The work presented is the result of a fruitful collaboration between many people.

It is a pleasure to thank Juan José Gómez Cadenas for his guiding, passionate involvement and almost-infinite patience. I wish to thank Pilar Hernández Gamazo for her profound insights and good advice; her efforts have beautifully combined with Juan José's to pave the way leading to the main contributions that our group has made to the field. My thanks also go to the other members of the group, who have provided a friendly environment and useful discussions during these years: Anselmo Cervera Villanueva, Jose Ángel Hernando Morata, Ana Tornero López and Gabriel Vidal Sitjes.

Most of the Monte Carlo inputs for water Cerenkov detectors come from David Casper, and the Monte Carlo simulation of the SPL neutrino beam from Alain Blondel and Simone Giani. To them I also express my gratitude.

I wish to thank all the contributors to this big enterprise that is science, who make understanding this world a little easier for everyone. In the same spirit, my thanks extend to all the Free Software contributors, who put at everyone's disposal the most valuable tool that humans have created: the computer. Both fields have introduced me to the joy of understanding and the pleasure of sharing.

Last but not least, I thank the support of my friends, Sara Gil Casanova, Jose Manuel Martí Martínez and Manuel Cifrián Pérez, and the always inspiring example of Joaquín D'Opazo Álvarez. To all of them, I am grateful beyond what any of my words could express.

BIBLIOGRAPHY

- [1] W. Pauli, “Fhünf Arbeiten zum Ausschliessungsprinzip und zum Neutrino,” Wissenschaftliche Buchgesellschaft Darmstadt (1977).
- [2] F. Reines and C. L. Cowan, “A Proposed Experiment To Detect The Free Neutrino,” *Phys. Rev.* **90** (1953) 492.
- [3] B. Pontecorvo, “Mesonium And Antimesonium,” *Sov. Phys. JETP* **6** (1957) 429 [*Zh. Eksp. Teor. Fiz.* **33** (1957) 549]
- [4] Z. Maki, M. Nakagawa and S. Sakata, “Remarks On The Unified Model Of Elementary Particles,” *Prog. Theor. Phys.* **28** (1962) 870.
- [5] J. N. Bahcall, P. I. Krastev and A. Y. Smirnov, “Where do we stand with solar neutrino oscillations?,” *Phys. Rev. D* **58** (1998) 096016
- [6] R. J. Davis, D. S. Harmer and K. C. Hoffman, “Search For Neutrinos From The Sun,” *Phys. Rev. Lett.* **20** (1968) 1205.
- [7] B. Richter, “Conventional beams or neutrino factories: The next generation of accelerator-based neutrino experiments,” arXiv:hep-ph/0008222.
- [8] W. Hampel *et al.* [GALLEX Collaboration], “GALLEX solar neutrino observations: Results for GALLEX IV,” *Phys. Lett. B* **447** (1999) 127.
- [9] J. N. Abdurashitov *et al.* [SAGE Collaboration], “Measurement of the solar neutrino capture rate by SAGE and implications for neutrino oscillations in vacuum,” *Phys. Rev. Lett.* **83** (1999) 4686.
- [10] T. Kajita [Super-Kamiokande Collaboration], “Atmospheric neutrino results from Super-Kamiokande and Kamiokande: Evidence for nu/mu oscillations,” *Nucl. Phys. Proc. Suppl.* **77** (1999) 123
- [11] Q. R. Ahmad *et al.* [SNO Collaboration], “Measurement of the charged current interactions produced by B-8 solar neutrinos at the Sudbury Neutrino Observatory,” *Phys. Rev. Lett.* **87** (2001) 071301

-
- [12] D. G. Koshkarev, "Proposal For A Decay Ring To Produce Intense Secondary Particle Beams At The Sps," CERN/ISR-DI/74-62.
- [13] K. Eguchi *et al.* [KamLAND Collaboration], "First results from KamLAND: Evidence for reactor anti-neutrino disappearance," *Phys. Rev. Lett.* **90** (2003) 021802 [arXiv:hep-ex/0212021].
- [14] S. N. Ahmed *et al.* [SNO Collaboration], "Measurement of the total active B-8 solar neutrino flux at the Sudbury Neutrino Observatory with enhanced neutral current sensitivity," arXiv:nucl-ex/0309004.
- [15] S. Geer, "Neutrino beams from muon storage rings: Characteristics and physics potential," *Phys. Rev. D* **57** (1998) 6989 [Erratum-ibid. *D* **59** (1999) 039903] [arXiv:hep-ph/9712290].
- [16] A. De Rujula, M. B. Gavela and P. Hernandez, "Neutrino oscillation physics with a neutrino factory," *Nucl. Phys. B* **547** (1999) 21 [arXiv:hep-ph/9811390].
- [17] A. Donini, D. Meloni and P. Migliozzi, "The silver channel at the neutrino factory," *Nucl. Phys. B* **646** (2002) 321 [arXiv:hep-ph/0206034].
- [18] M. Freund, P. Huber and M. Lindner, "Systematic exploration of the neutrino factory parameter space including errors and correlations," *Nucl. Phys. B* **615** (2001) 331 [arXiv:hep-ph/0105071].
- [19] P. Huber, M. Lindner and W. Winter, "Superbeams versus neutrino factories," *Nucl. Phys. B* **645** (2002) 3 [arXiv:hep-ph/0204352].
- [20] V. Barger, D. Marfatia and K. Whisnant, "Off-axis beams and detector clusters: Resolving neutrino parameter degeneracies," *Phys. Rev. D* **66** (2002) 053007 [arXiv:hep-ph/0206038].
- [21] V. Barger, D. Marfatia and K. Whisnant, "Breaking eight-fold degeneracies in neutrino CP violation, mixing, and mass hierarchy," *Phys. Rev. D* **65** (2002) 073023 [arXiv:hep-ph/0112119].
- [22] J. Burguet-Castell, M. B. Gavela, J. J. Gomez-Cadenas, P. Hernandez and O. Mena, "On the measurement of leptonic CP violation," *Nucl. Phys. B* **608** (2001) 301 [arXiv:hep-ph/0103258].

APPENDIX

A. PROGRAM ARCHITECTURE AND COMPUTER-RELATED TOOLS

A.1 *Numerical Simulations*

To make a realistic study of the future experiments performance, an intensive numerical simulation is ultimately needed.

First, the initial flux must be well known, which in the case of the Neutrino Factory implies just using the easily-derived formulas, but for Superbeams it requires a full Monte Carlo simulation. The fluxes must be then correctly extrapolated to the detector, using the exact oscillation formulas, and taking into account matter effects, which implies diagonalizing the hermitian mass matrix. The number of events recorded in the detector must be evaluated knowing the different cross-sections involved; knowing them and estimating both the efficiencies and the background rejection factors typically imply tough Monte Carlo simulation. Finally, all this process must be done for all the allowed parameter space, to get the χ^2 functions that allow for the reconstruction of the oscillation parameters, or to see the sensitivity to them.

A.2 *Implementation*

To address the numerical simulations a set of programs have been developed during the realization of these studies. The results of the Monte Carlo simulations of the neutrino source and the detector have been taken from external sources. For all the rest, the programs that have been developed account for more than 20000 (2×10^4 ...) lines of code.

Because the parameter space is very large, a big effort has been made to create programs that are as efficient as possible. We chose to program in C++ to make use of its highly optimized binary output, at the same time that it allows us to decompose naturally the problem of the simulation by means of Object-Oriented Programming techniques.

A.3 Architecture

A.3.1 Generation of Data

Our simulations have addressed different kind of neutrino experiments (the Neutrino Factory and the SPL-Superbeam most relevantly, but also the JHF-Superbeam and Betabeams, which are not discussed in this work), and from them we were able to find a common structure that allows us to reuse much of the work from one simulation to others.

We have defined classes with fixed interfaces. For illustration with a simplified model, the main relationship takes place between the *Source*, which contains all the relevant information about the neutrino beam source, the *Detector*, that knows about cross sections and efficiencies, and an *Experiment*, which is formed by a Source and a Detector placed at some distance.

- Source: $\left(\frac{d^2 N_i}{dE d\Omega}\right)_{source}$
- Detector: σ_i (cross sections), ϵ_i (efficiencies).
- Experiment:

$$\begin{aligned} \left(\frac{d^2 N_i}{dE dS}\right)_{exp} &= \sum_j \frac{1}{L^2} \times \left(\frac{d^2 N_j}{dE d\Omega}\right)_{source} \times P_{j \rightsquigarrow i} \\ \left(\frac{dN_i}{dS}\right)_{exp} &= \int \left(\frac{d^2 N_i}{dE dS}\right)_{exp} dE \\ \frac{dN_{evt i}}{dE} &= \epsilon_i \times \left(\frac{d^2 N_i}{dE dS}\right)_{exp} \times \sigma_i \\ N_{evt i} &= \int \frac{dN_{evt i}}{dE} dE \end{aligned}$$

A.3.2 Reconstruction

A χ^2 -based study usually follows the generation of the large datasets for the observables in a neutrino experiment. Our current structure for the reconstruction of oscillation parameters is based on a library that we have developed. In it, an object of the type *AnalysisKernel* gathers all the information needed and handles interpolations transparently, so the user can request the χ^2 fits for a given set of values directly and in a flexible way.

This approach has allowed us to develop graphical user interfaces (GUIs) to make many of the analysis more responsive and intuitive. The decouple of the kernel and the GUI also permits to use the kernel directly in more time-consuming analysis that can last for hours or days.

A.4 Software Tools

To develop our programs we have made extensive use of Free Software, which allows anyone to use them without having to pay for expensive numerical libraries or accepting unfair licensing terms.

In particular, we have much profited from

- The GNU Scientific Library (GSL) (<http://sources.redhat.com/gsl/>)
Provides a well-defined C language Applications Programming Interface for common numerical functions.
- Qt (<http://www.trolltech.com/products/qt/index.html>)
A multiplatform C++ graphics library.

as well as many utilities like *gnuplot*, *emacs*, *gcc* and *CVS* to mention only a few.

A.5 Availability

All our programs are publicly available through anonymous access to our CVS repository. The instructions can be found in <http://evalu29.uv.es/software/>

Several persons have already showed their interest in using the programs we have developed. We are very pleased for it, and would like to continue encouraging this practice.